NASA/TP–20230006226
NESC-RP-21-01721

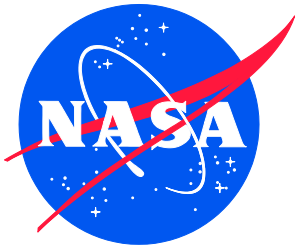

Evaluation of Through-thickness Microtextural Characteristics in 2219-T87 Thick Plate

Stephen J. Hales, and Wesley A. Tayon
Langley Research Center, Hampton, Virginia

April 2023

NASA STI Program Report Series

Since its founding, NASA has been dedicated to the advancement of aeronautics and space science. The NASA scientific and technical information (STI) program plays a key part in helping NASA maintain this important role.

The NASA STI program operates under the auspices of the Agency Chief Information Officer. It collects, organizes, provides for archiving, and disseminates NASA's STI. The NASA STI program provides access to the NTRS Registered and its public interface, the NASA Technical Reports Server, thus providing one of the largest collections of aeronautical and space science STI in the world. Results are published in both non-NASA channels and by NASA in the NASA STI Report Series, which includes the following report types:

- TECHNICAL PUBLICATION. Reports of completed research or a major significant phase of research that present the results of NASA Programs and include extensive data or theoretical analysis. Includes compilations of significant scientific and technical data and information deemed to be of continuing reference value. NASA counterpart of peer-reviewed formal professional papers but has less stringent limitations on manuscript length and extent of graphic presentations.

- TECHNICAL MEMORANDUM. Scientific and technical findings that are preliminary or of specialized interest, e.g., quick release reports, working papers, and bibliographies that contain minimal annotation. Does not contain extensive analysis.

- CONTRACTOR REPORT. Scientific and technical findings by NASA-sponsored contractors and grantees.

- CONFERENCE PUBLICATION. Collected papers from scientific and technical conferences, symposia, seminars, or other meetings sponsored or co-sponsored by NASA.

- SPECIAL PUBLICATION. Scientific, technical, or historical information from NASA programs, projects, and missions, often concerned with subjects having substantial public interest.

- TECHNICAL TRANSLATION. English-language translations of foreign scientific and technical material pertinent to NASA's mission.

Specialized services also include organizing and publishing research results, distributing specialized research announcements and feeds, providing information desk and personal search support, and enabling data exchange services.

For more information about the NASA STI program, see the following:

- Access the NASA STI program home page at http://www.sti.nasa.gov

- Help desk contact information:

https://www.sti.nasa.gov/sti-contact-form/
and select the "General" help request type.

NASA/TP–20230006226
NESC-RP-21-01721

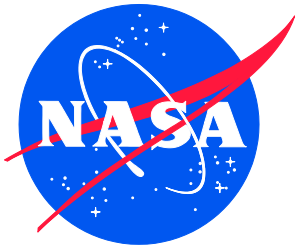

Evaluation of Through-thickness Microtextural Characteristics in 2219-T87 Thick Plate

Stephen J. Hales, and Wesley A. Tayon
Langley Research Center, Hampton, Virginia

National Aeronautics and
Space Administration

Langley Research Center
Hampton, Virginia 23681-2199

April 2023

Acknowledgments

Manuscript reviews; Prof. Armand J. Beaudoin, Department of Mechanical Engineering, University of Illinois, Urbana, IL.
Prof. Anthony D. Rollett, Department of Materials Science and Engineering, Carnegie Mellon University, Pittsburgh, PA.

EBSD data acquisition; Peter J. Bonacuse, Aerospace Materials, NASA Glenn Research Center, Cleveland, OH.

Metallographic data acquisition; W. Matt Medders, Materials Science and Metallurgy Branch, NASA Marshall Space Flight Center, Redstone Arsenal, AL.

Data analysis; David E. Stegall, Ph.D., Advanced Materials and Processing Branch, NASA Langley Research Center, Hampton, VA.

The reader is referred to the sister publication;

S.J. Hales, ***Metallurgical Factors that Govern ST Properties in Commercial 2219-T87 Thick Plate***, NASA/TM–20230006220, NASA Engineering & Safety Center, Langley Research Center, Hampton, VA, 18 pp., April 2023.

The use of trademarks or names of manufacturers in the report is for accurate reporting and does not constitute an official endorsement, either expressed or implied, of such products or manufacturers by the National Aeronautics and Space Administration.

Available from:

NASA STI Program / Mail Stop 148
NASA Langley Research Center
Hampton, VA 23681-2199
Fax: 757-864-6500

Preface

This study concluded that the effects of crystallographic texture on the variability of short-transverse (ST) ductility in recrystallized 12.7-cm-thick 2219-T87 plate (lot 930081-726) are complementary to the effects of grain boundary (GB) precipitates. The most probable root cause is the cross-sectional profile of Cu macro-segregation in the high-solute alloy. The resultant inhomogeneous distribution of coarse Al_2Cu θ-phase controls particle-stimulated nucleation (PSN) of new grains during subsequent thermomechanical processing. In turn, this mechanism governs texture asymmetry, grain orientation distributions, and grain boundary characteristics, which can increase susceptibility to intergranular fracture. Considering processing history, this sequence of events likely stems from issues with casting practice, specifically quenching and homogenization treatments.

Microtexture analysis reveals that through-thickness gradients in the composition and spatial distribution of individual components are complex. The data do suggest a possible relationship between grain size and textural characteristics through the cross-section, particularly adjacent to the plate surfaces. The general trend comprises location-dependent increases in recrystallized grain orientations countered by decreases in deformed grain orientations. The overall texture is weak, such that the cross-sectional variations noted (see Appendix A) are not classified as a first-order effect on ST ductility and/or fracture behavior.

Electron backscatter diffraction (EBSD) analyses clearly demonstrate that the cross-sectional variations in microtextural characteristics are asymmetrical within the plate. This result does highlight the importance of not assuming that the microstructure of thick plate is symmetrical in either the short- or long-transverse directions. It is encouraged that similar investigations prioritize the compilation of microtextural data representative of the entire cross-section in Al alloy rolled products. The novel analytical treatments of a single dataset, as applied in this case, may provide a template for efficient microtexture analysis of multiple datasets in the future.

Table of Contents

List of Figures

List of Tables

Nomenclature

A_f	area fraction (texture components)
AR	aspect ratio (grain dimensions)
ASTM	American Society for Testing and Materials
CSL	coincident site lattice (boundary)
DC	direct chill (semi-continuous casting)
DEF	deformation-related (texture)
$\overline{\mathbf{d}}_P$	average particle diameter (θ-phase)
EBSD	electron backscatter diffraction (analysis)
EDM	electrical discharge machining
El.	elongation-to-fracture (tensile ductility)
GB	grain boundary
GRC	Glenn Research Center (NASA)
$\overline{\mathbf{g}}_L$	average longitudinal grain dimension (// to RD)
$\overline{\mathbf{g}}_S$	average short-transverse grain dimension (// to ND)
IPF	inverse pole figure (plots and maps)
L	longitudinal (direction)
L_f	length fraction (grain boundaries)
L-LT	plane containing L and LT directions (RD-TD)
L-ST	plane containing L and ST directions (RD-ND)
LT	long-transverse (direction)
LaRC	Langley Research Center (NASA)
MDF	misorientation distribution function (boundaries)
ND	normal direction (// to ST)
ODF	orientation distribution function (analysis)
PSN	particle-stimulated nucleation
RD	rolling direction (// to L)
REX	recrystallization-related (texture)
RX	recrystallization
SEM	scanning electron microscope
ST	short-transverse (direction)
Σ	sigma value (CSL boundaries)
$\boldsymbol{\sigma}_{UTS}$	ultimate tensile strength
$\boldsymbol{\sigma}_{YS}$	tensile yield strength
TD	transverse direction (// to LT)

1.0 Introduction

1.1 Role of Crystallographic Texture

The primary objective of this study was to establish if crystallographic texture played a major role in variable ductility in the short-transverse (ST) direction of 12.7-cm-thick 2219-T87 plate (lot 930081-726). The broader investigation revealed a long-transverse (LT) variation in the ST tensile properties, i.e. between the edge and center of multiple other lots. As shown in Table 1, the average elongation-to-fracture was $\overline{El.}$ = 4.4 % at the edge, but only $\overline{El.}$ = 2.0 % at the center of the plates during ASTM E8 testing [data courtesy of Medders]. Importantly, it was observed that the full-thickness specimens tended to fail at ≈ t/2 by transgranular fracture at the edge, but at ≈ 3t/8 by intergranular fracture at the center of the plate. It was surmised that through-thickness variations in the size and distribution of the Al_2Cu θ-phase on GBs were primarily responsible. Such cross-sectional variations in grain structure or texture are common and depend on both casting practice and rolling procedures [ref. 1]. Accordingly, a secondary objective was an assessment of the possible effects of processing history on microstructural variations through the plate.

Table 1. Long-transverse (LT) variations in the short-transverse (ST) tensile properties of the lots of 12.7-cm-thick 2219-T87 plate included in this investigation [data courtesy of Medders].

Vendor	Lot #	Cut Plan #	Transverse Location	Short-Transverse (ST) Tensile Properties		
				σ_{UTS} (MPa)	σ_{YS} (MPa)	El. (%)
ARCONIC	376441	*LTI-A2*	NA	415	387	1.6
	420612	*LTI-A1*	NA	415	383	1.8
	420612	725	Center	446	387	3.0
			Edge	469	388	5.6
CONSTELLIUM	930071	*LTI-C1*	NA	392	358	1.7
	930071	722	Center	391	361	1.5
			Edge	448	370	4.4
	930081	726	Center	386	353	1.5
			Edge	425	354	3.3
	930082	723	Center	398	359	2.0
			Edge	443	364	4.3
	9492854	720	NA	452	367	6.3
Average values for elongation-to-fracture: $El._{Edge}$ = 4.4 % and $El._{Center}$ = 2.0 %						

Customarily, the industrial manufacturing of Al alloy plate involves direct chill (DC) casting, followed by break-down and finish rolling. Semi-continuous DC casting usually causes solute gradients in the LT and ST directions of the billet; the general trend comprising a lower solute content at the core than the outer surfaces [ref. 2]. In high-solute alloys, such as Al 2219, this

characteristic makes quenching and homogenization procedures critical to mechanical property uniformity [refs. 4 and 5]. Transverse macro-segregation of Cu tends to be an unrecoverable feature that becomes more prominent with scale, such that any effects are 'inherited' by subsequent thermomechanical processing steps [ref. 5]. Hot rolling deformation modifies the texture and introduces textural gradients in the ST direction that can promote mechanical anisotropy in the final product [ref. 6]. As a consequence, the analytical philosophy adopted was to evaluate whether cross-sectional gradients in microtextural features were sufficient to influence fracture location and compromise ST ductility. Electron backscatter diffraction (EBSD) analysis, a powerful scanning electron microscopy (SEM) tool, was deployed to provide quantitative information as a function of location within the plate.

1.2 Rolling, Shear, and Recrystallization Components

Crystallographic texture can be fractionated into individual components in Euler space using orientation distribution function (ODF) analysis [ref. 7]. EBSD techniques quantify the composition and spatial distribution of location-dependent microtexture characteristics. The textural composition of Al alloy wrought product can conveniently be divided into deformation-related (DEF) and recrystallization-related (REX) components [ref. 8]. The DEF components of rolled product can be sub-divided into rolling- and shear-related components that usually exhibit cross-sectional gradients in intensity [ref. 9].

At first glance, deformation by rolling would appear to be symmetric in nature. However, several attributes of the process can readily lead to cross-sectional texture asymmetry in practice [refs. 11 and 12]. Texture is very sensitive to the friction coefficient between the workpiece and roller surfaces, which can differ for the top and bottom work rolls in commercial mills [ref. 6]. A common characteristic of the rolling process is a continuously decreasing ratio of shear over compressive strain from both surfaces toward the mid-plane [ref. 12]. In sheet product, through-thickness gradients in microtextural composition and distribution are often symmetric about the mid-plane and less severe in recrystallized material. However, lower thickness reductions for thick plate product dictate that heterogeneities in the DC cast billet are more likely to be retained [ref. 13].

ODF analysis is most effective when commonly accepted nomenclature, Miller indices, and Euler angles of individual texture components are employed (Table 2) [refs. 11 and 15]. The rolling components consist of intensities along the β-fiber, connecting the ***Bs*** with ***Cu*** orientation and traversing ***S*** and ***S*** variants (***S′***). The shear components tend to comprise intensities along the <110>-fiber (***E***, ***H***, ***I***), but can also include ***F*** and the cross-rolling ($\boldsymbol{X_R}$) orientations . The REX components usually consist of ***Cube*** or rotated-cube (***RC***) orientations, manifested as intensities along the <100>-fiber ({hkl}<100>rotated about RD) and <001>-fiber ({001}<uvw> rotated about ND). Many REX components are also associated with nucleation at localized microstructural inhomogeneities, such as transition bands, shear bands and second phase particles [ref. 15]. The presence of texture components related to PSN may be particularly significant due to the abundance and variability of intergranular θ-phase already noted in this investigation.

The PSN concept addresses heterogeneous deformation and the origin of RX, where second phase particles create highly localized regions of increased strain [ref. 16]. The theory suggests that PSN occurs above a critical particle size (1-2 μm) and the final grain size and shape is commensurate with the interparticle spacing. The grain orientations that are frequently associated with the PSN mechanism are the ***Cube***, $\boldsymbol{RC_{ND}}$, $\boldsymbol{RC_{RD}}$, ***P***, and ***Q*** texture components [ref. 17]. The structure of

GBs resulting from the formation of these grain orientations may affect the propensity for intergranular fracture. In this case, the size of recrystallized grains nucleated at θ-phase will be governed by the particle size and spacing on existing GBs. A non-uniform particle size and distribution will tend to promote microstructural variability, i.e. a mixture of grain sizes and morphologies. In other lots of Al 2219 plate, average particle sizes of 24-27 μm^2 at 3t/8 ($\bar{d}_P \approx 5.7$ μm) and 5-7 μm^2 at t/2 ($\bar{d}_P \approx 2.8$ μm) for the θ-phase have been documented, both exhibiting low ST ductility [data courtesy of Medders].

Table 2. The texture components selected for ODF analysis. Individual components are separated into rolling, shear and RX categories for this study. The common nomenclature, Miller indices and Euler angles (Bunge) are shown.

Texture Components		Miller Indices		Euler Angles (Bunge)		
		{hkl}	<uvw>	φ_1	ϕ	φ_2
ROLLING	Bs	011	211	35	45	0
	S	123	634	55	35	65
	S'_1	123	412	25	60	20
	S'_2	146	211	55	85	35
	Cu	112	111	90	30	45
SHEAR	X_R	011	322	45	45	0
	E	111	110	0	55	45
	F	111	211	90	55	45
	H	001	110	0	0	45
	I	112	110	0	35	45
RECRYSTALLIZATION	Goss	011	100	0	45	0
	Cube	001	100	0	0	0
	RC_{RD1}	013	100	0	20	0
	RC_{RD2}	023	100	0	35	0
	RC_{ND1}	001	310	20	0	0
	RC_{ND2}	001	320	35	0	0
	P	011	122	70	45	0
	Q	013	231	55	20	0
	R	124	211	55	75	25
	Bs_{RX}	113	211	75	25	45

Individual grains act like single crystals and, thus, exhibit anisotropic mechanical behavior. When confined in a polycrystalline aggregate, the microtextural composition determines the bulk

anisotropy. DEF textures can magnify the resolved shear stresses acting on GBs and accelerate strain localization [ref. 18]. In unrecrystallized wrought Al product, yield strength directionality can readily be correlated with textural composition via Taylor factor analysis [ref. 19]. The microtextural distribution also influences the network of GBs within a grain structure via the intersection of varying lattice orientations. ODF data acquired via EBSD not only provide the area fractions of grains with a given orientation, but also the length of GBs with given misorientations. Texture gradients can exert a significant influence on ST properties in elongated grain structures, because a large areal fraction of flat GBs is physically oriented in the RD-TD plane [ref. 20]. Variations in GB characteristics in the current plate product are important, because reduced ST ductility may be related to a transition from trans- to inter-granular fracture.

1.3 Grain Boundary Characteristics

Select GBs within a network can be also categorized as 'special boundaries', which are known as coincident site lattice (CSL) boundaries. The CSL concept is a geometrical classification of the intersection of adjacent lattices at a planar interface [ref. 21]. The sigma (Σ) value is the reciprocal of periodic registry between the adjoining lattices, i.e. one-in-every-three sites coincide for a Σ3 boundary. The misorientation for each type of CSL boundary is uniquely defined by crystallographic axis/angle pairs, e.g. Σ3 is 60°∧<111>. The formation and properties of CSL boundaries can be associated with both discrete RX phenomena and the physical integrity of GBs [ref. 22]. For example, GBs separating neighboring 'hard'- and 'soft'- oriented grains can be susceptible to intergranular fracture in strong-textured and unrecrystallized Al rolled product [ref. 23]. However, such an effect is minimal in weak-textured and recrystallized wrought product because mechanical behavior tends to be more isotropic [ref. 18].

The structural integrity of GBs not only depends on the physical orientation of the GB planes and the misorientation angle between adjacent grains, but also the interfacial character of the GBs [ref. 24]. Geometric CSLs are planar interfaces and the structure of non-planar GBs contains alternating regions of coincidence and disorder, often in the form of discrete steps. It has been surmised that GBs containing low CSL designations exhibit increased resistance to intergranular fracture compared with random boundaries [ref. 25]. High coincident site density may have more relevance to the elongated grain structures typical of Al 2219 plate. The significant areal fraction of planar GBs residing in the rolling plane may comprise single CSLs and increase the significance of Σ3, Σ5, Σ7, and Σ9 lineal densities. GB energy is also governed by the interfacial character, which can affect nucleation and growth of intergranular θ-phase. The resultant through-thickness variations in GB precipitates may culminate in a location-dependent influence on susceptibility to intergranular fracture.

2.0 Experimental Procedures

This EBSD study involved data collection and grain structure analysis at NASA Glenn Research Center (GRC) and ODF analysis of texture on imported data at NASA Langley Research Center (LaRC). ***AZtecHKL™*** acquisition software by Oxford Instruments [ref. 26] was used for inverse pole figure mapping with ND as the reference axis (IPF_{ND}) in order to quantify the grain size and morphology. ***OIM Analysis™*** software by EDAX [ref. 27] was used to generate ODF plots for quantifying the crystallographic texture composition/distribution and GB characteristics. The specimen examined was a full-thickness section extracted from the center of a piece of 12.7-cm-thick 2219-T87 plate (lot 930081-726).

2.1 EBSD at Glenn Research Center

At NASA-GRC, wire EDM was employed to excise the ≈ 127 mm long by ≈ 25 mm wide by ≈ 16 mm thick sample, corresponding with the ST, L, and LT directions in the rolled plate (Figure 1(a)). Attention was paid to removing sufficient material during specimen preparation to eliminate any effects due to the EDM re-cast layer. The surface for analysis (L-ST plane) was prepared for EBSD by manual sanding with silicon carbide paper, followed by rotary polishing on cloth with successively finer diamond suspensions (9, 6, 3, and 1 μm), and finished by vibratory polishing with 0.05 μm colloidal silica.

The EBSD data were collected using a Tescan MAIA3 SEM operated at an accelerating voltage of 20 kV. The system was equipped with an Oxford Instruments NordlysNano EBSD detector operated with ***HKL*** software. The dimensions of the IPF mapping areas were 2.82 mm (L direction) x 2.11 mm (ST direction), with a sampling step size of 10 μm (resolution; 283 x 212 pixels, patterns; 59,996). As shown in Figure 1(b), the through-thickness locations selected for data acquisition were t/8, t/4, 3t/8, t/2 (2), 5t/8, 3t/4, and 7t/8 (Note that cross-sectional texture symmetry was not assumed).

The numerical coordinates employed for automated data collection and the specimen orientation axes are indicated. IPF_{ND} maps were used to determine the location-dependent grain size and morphology in the plate cross-section. Standards for EBSD analysis of both grain size [ref. 28] and grain orientation [ref. 29], distributions recommend sampling > 500 grains per location for statistical accuracy. The average length along RD ($\bar{g}L$) and the RD:ND aspect ratio ($\bar{g}L/\bar{g}S$) were evaluated from a sampling of ≈ 600 grains per through-thickness location. 'Border grains' clipped by the perimeter of the sampling area were eliminated from the analyses.

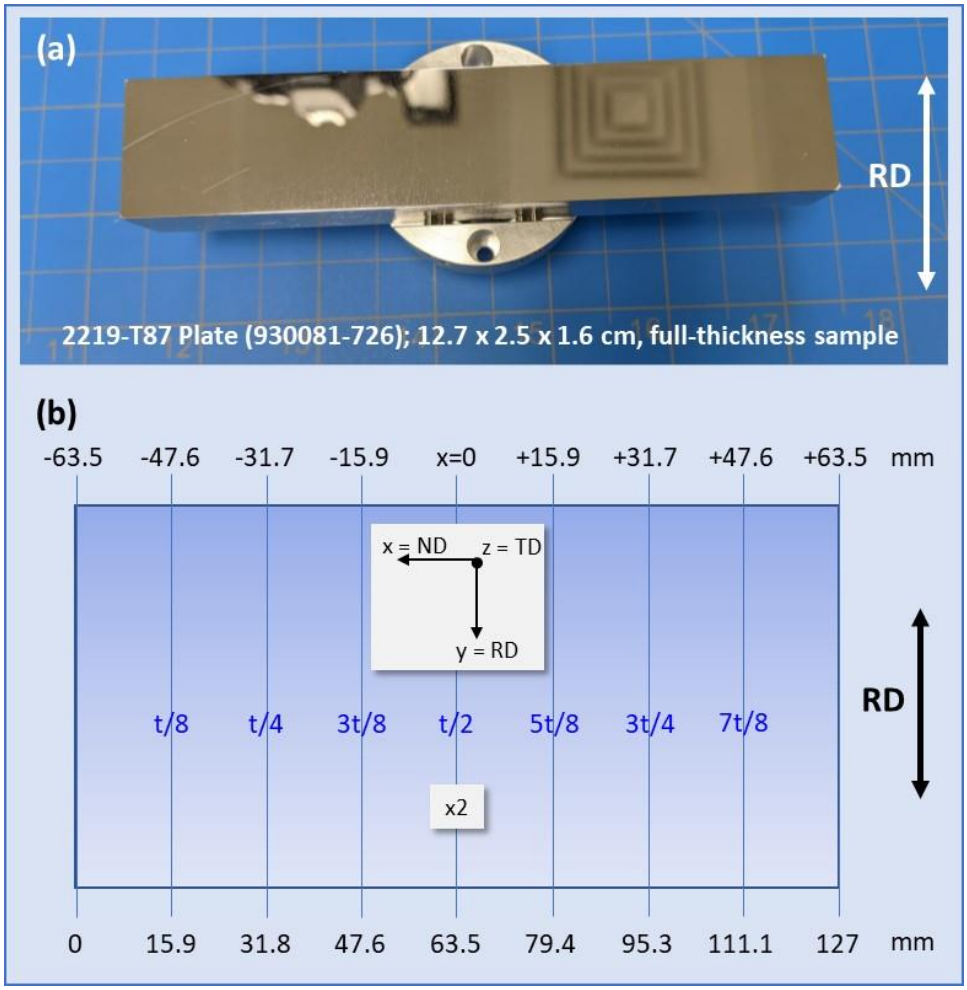

Figure 1. The protocol for EBSD data collection from the 12.7-cm-thick 2219-T87 plate (930081-726) adopted in this study; (a) specimen orientation and dimensions; (b) numerical coordinates, reference frame and through-thickness locations for data acquisition.

2.2 EBSD Analyses at Langley Research Center

At NASA-LaRC, the raw data acquired //TD using the ***HKL*** software were manipulated for ODF analysis //ND using the ***OIM*** software. This required a double 90° rotation in Euler space to align both the scan normal and raster direction. ODF plots using the Bunge notation were used to quantify the microtextural features through the plate cross-section [ref. 7]. Microtextural analyses evaluated the composition and spatial distribution of both grain orientations and GB characteristics with respect to the customary set of specimen axes.

The EBSD analysis focused on evaluating microstructural and textural differences that might influence the variability in ST ductility and fracture behavior. Full thickness tensile specimens extracted from the center of the 12.7-cm-thick 2219-T87 plate (lot 930081-726) broke at 3t/8 (or 5t/8) with El.= 1.5 %, presumably by intergranular fracture. The 3t/8 and 5t/8 through-thickness locations were indistinguishable because the 'top' and 'bottom' of the plate were not identified through most of this investigation. Therefore, data compiled at the 3t/8 and 5t/8 locations were compared with the data compiled at the two t/2 locations ($t/2_I$ and $t/2_{II}$).

The LaRC analysis of the GRC data assumed a three-pronged approach;

- The first provided the composition of grain orientations at each of the through-thickness locations. The data were examined relative to cross-sectional symmetry (t/8 to 7t/8) and the common fracture locations (3t/8, t/2, and 5t/8). The results were interpreted based on the frequency of specific texture components within the rolling-, shear- and RX-related categories.
- The second included a novel treatment of the spatial distribution data at select through-thickness locations. The procedure involved distillation of the full-spectrum IPF maps down to grains oriented in close proximity to the primary {hkl} and <uvw> directions (Table 3). Four-color mapping of the <100>, <110>, <111>, and <211> 'texture fibers' placed emphasis on the RX, shear, and rolling categories. Consequently, data were compiled as area fractions of 'families' of grain orientations.
- The third provided the composition and spatial distribution of GB characteristics at the common fracture locations. Plotting the misorientation distribution function (MDF) revealed the frequency of GB misorientations in the 15° to 65° range. The data were compared with the theoretical random distribution and the rotation angles for specific CSL boundaries. Mapping of the GB network was fractionated by misorientation angle between 15° to 65°, binned into 10° angular increments. GB types were sub-divided into length fractions of CSL boundaries using the axis/angle pairs defined in Table 4. Data were compiled as location-dependent length fractions of GB misorientations and CSLs.

Table 3. Distillation of full-spectrum IPF maps down to four-color IPF_{ND} and IPF_{RD} maps highlights groups of grains oriented in proximity to the constituent {hkl} and <uvw> directions. Mapping of the primary <001>, <011>, <111>, and <211> texture fibers emphasizes the RX, shear, and rolling categories.

Distilled Map Type	Components in Vicinity of Texture Fibers			
	20°^ <001>	15°^ <011>	15°^ <111>	10°^ <211>
IPF_{ND} {hkl}	*H* *Cube* RC_{RD1} RC_{ND1} RC_{ND2} *Q*	*Bs* X_R *Goss* RC_{RD2} *P*	*E* *F*	*Cu* *I* Bs_{RX}
IPF_{RD} <uvw>	*Goss* *Cube* RC_{RD1} RC_{RD2} RC_{ND1}	*E* *H* *I* RC_{ND2}	*Cu* X_R *P*	*Bs* *S* S'_1 S'_2 *F* *R* Bs_{RX}

Table 4. List of coincident site lattice (CSL) boundaries indicating specific axis/angle pairs with misorientations between 15° and 60° angular rotation and the associated Σ designations [ref. 21].

Angle, °	Axis, <hkl>	Σ value	Angle, °	Axis, <hkl>	Σ value
18	111	31b	39	110	9
22	111	21a	41	210	41b
27	110	19a	44	211	21b
28	111	13b	48	210	15
35	210	27b	50	110	11
37	100	5	55	320	31a
38	111	7	60	111	3

3.0 Results of EBSD Analyses

3.1 Cross-sectional Microtexture Asymmetry

The first objective of the EBSD analysis was to evaluate cross-sectional variations in grain structure and texture at the center of the 12.7-cm-thick 2219-T87 plate (lot 930081-726). The results of full spectrum IPF_{ND} mapping in Figure 2 reveal that the grain size and morphology in the L-ST plane are fairly uniform in the plate mid-section, but become coarser and more elongated towards the plate surfaces. The increase in grain length/aspect ratio is most pronounced from t/4 to t/8, and from 3t/4 to 7t/8. The data in Figure 3(a) indicate that the average grain area of 6,842 μm^2 between 3t/8 and 5t/8 (location of fracture) increases to 10,039 μm^2 at t/8 and 7t/8. The data in Figure 4 show that the variability in grain area approximates a unimodal distribution at all of the through-thickness locations. Consequently, the average dimensions of the elongated grain structure are statistically significant; $\bar{g}_L$ = 165 µm / $\bar{g}_{ST}$ = 53 µm in the mid-section (3t/8 to 5t/8) increases to $\bar{g}_L$ = 212 µm / $\bar{g}_{ST}$ = 58 µm towards the surfaces (t/8 and 7t/8).

The relative area fractions of the selected texture components are presented in Table 5 as a function of through-thickness location in the plate. The contributions of the individual components are divided into rolling, shear, and RX categories. The tabulated data indicate that the overall texture intensity is weak across most of the cross-section and RX is the predominant category. The 'total' area fraction indicates that the analysis accounts for $A_f > 90\%$ of the textural composition in the plate cross-section. Summation of the individual components in Table 5 reveals the variation in the rolling, shear, and RX categories as a function of through-thickness location presented in Figure 5 and Table 6. In Figure 5, variations in all three categories are symmetrical about the mid-plane between t/4 and 3t/4, but asymmetrical towards the plate surfaces, i.e. t/8 and 7t/8. The general through-thickness trend comprises decreasing RX, with slightly increasing shear and rolling, from t/8 to 7t/8. At t/8, $A_f \approx 68\%$ for RX, $A_f \approx 12\%$ for shear, $A_f \approx 15\%$ for rolling. At

7t/8, $A_f \approx 38\%$ for RX, $A_f \approx 23\%$ for shear, $A_f \approx 30\%$ for rolling. It is evident that RX is higher at t/2 than 3t/8 or 5t/8, whereas shear and rolling are lower at t/2 than 3t/8 or 5t/8. In Table 6, the RX category provides the major contribution, with the shear and rolling categories providing lesser contributions at t/8 and t/2. However, the relative contributions are more evenly matched at the 7t/8 location, further highlighting the textural asymmetry through the plate.

The area fractions of the texture components that constitute the rolling, shear, and RX categories are plotted as separate groups in Figure 6. It is readily apparent that the through-thickness variations in all of the individual components are very complicated and comprise differing cross-sectional profiles. Accepting that some of the variability may be a consequence of the limited scanning area for each orientation map, the details are as follows;

- Rolling components (Figure 6(a)); Along the β-fiber, $\boldsymbol{S'_2}$ is most prominent over the cross-section and varies asymmetrically about the mid-plane. $\boldsymbol{S'_2}$ trends downwards from t/4 to 3t/4 and then peaks at 7t/8. Among the lesser contributions, ***S*** trends slightly upwards from t/8 to 5t/8 and then peaks at 7t/8. Both $\boldsymbol{S'_2}$ and ***S*** exhibit a dip at 3t/4. $\boldsymbol{S'_1}$ exhibits through-thickness undulations with peaks at 3t/8 and 3t/4, and a valley between t/2 and 5t/8. ***Bs*** and ***Cu*** vary symmetrically about the mid-plane with minima at t/2.
- Shear components (Figure 6(b)); ***F*** and ***I*** are most prominent over the cross-section, both being higher at 7t/8 than t/8, and showing peaks at 3t/8 and 5t/8. ***E*** is the only component that varies symmetrically over the entire cross-section, peaking between 3t/8 and 5t/8. $\boldsymbol{X_R}$ has the most asymmetrical variation, showing a significant increase from t/2 to 7t/8. ***H*** is consistently low, but does show a peak at 3t/8 and a valley at t/4. Through-thickness variations of all components are almost symmetrical about the mid-plane between 3t/8 and 5t/8, and all dip at t/2.
- RX components (Figures 6(c)&(d)); ***Q*** is most prominent over the cross-section within the dominant RX category. The major contributions from ***Q***, $\boldsymbol{RC_{ND1}}$ and $\boldsymbol{RC_{RD1}}$ vary asymmetrically about the mid-plane. ***Q*** is strongest at t/8, $\boldsymbol{RC_{ND1}}$ is strongest between 3t/8 and t/2, and $\boldsymbol{RC_{RD1}}$ is strongest at t/2. Variations in the minor contributions from ***Cube*** , $\boldsymbol{RC_{RD2}}$, $\boldsymbol{RC_{ND2}}$, and ***P*** exhibit complex through-thickness patterns. ***Cube*** is strong at t/2, $\boldsymbol{RC_{RD2}}$ is strong at t/8 and 7t/8, $\boldsymbol{RC_{ND2}}$, is strong at 3t/8, and ***P*** is strong at t/4 and 3t/4. ***P*** is the only component that varies symmetrically about the mid-plane.

Complementary to quantification of microtextural composition, EBSD analysis was employed to quantify microtextural spatial distribution. Distilled IPF mapping restricted to the primary texture fibers, with either ND or RD as the normal orientation, isolated the {hkl} and <uvw> constituents. The IPF_{ND} and IPF_{RD} texture fiber maps are color coded according to 20°∧<001>, 15°∧<011>, 15°∧<111>, and 10°∧<211>. The individual texture components contained within these crystallographic vicinities are listed in Table 3. Examining data from the vicinity of both surfaces of the plate highlights the cross-sectional variation in the area fraction and arrangement of specific grain orientations.

The distilled IPF_{ND} and IPF_{RD} maps for the t/8 and 7t/8 locations shown in Figure 7 compare the microtextural features in the vicinity of the plate surfaces. The IPF_{ND} maps at t/8 and 7t/8 (Figures 7(a)&(c)) show that the area fractions of {001}-, {011}-, {111}- and {112}-oriented grains are A_f= 31%, 18%, 6%, and 15% at t/8, and A_f= 27%, 10%, 16%, and 21% at 7t/8. The {001} orientation, that can contain ***H***, ***Cube***, $\boldsymbol{RC_{RD1}}$, $\boldsymbol{RC_{ND1}}$, $\boldsymbol{RC_{ND2}}$, and ***Q***, dominates at both surfaces of the plate. The IPF_{RD} maps at t/8 and 7t/8 (Figures 7(b)&(d)) show that the area fractions of <100>-

, <110>-, <111>- and <211>-oriented grains are A_f= 15%, 28%, 5%, and 16% at t/8, and A_f= 15%, 12%, 23%, and 23% at 7t/8. The <110> orientation, that can contain ***E***, ***H***, ***I*** and RC_{ND2}, dominates adjacent to one surface (t/8). In contrast, the <111> orientation, that can contain ***Cu***, X_R, and ***P***, and the <211> orientation, that can contain ***Bs***, ***S***, S'_1, S'_2, ***F***, ***R***, and Bs_{RX}, are most prominent at the other surface (7t/8).

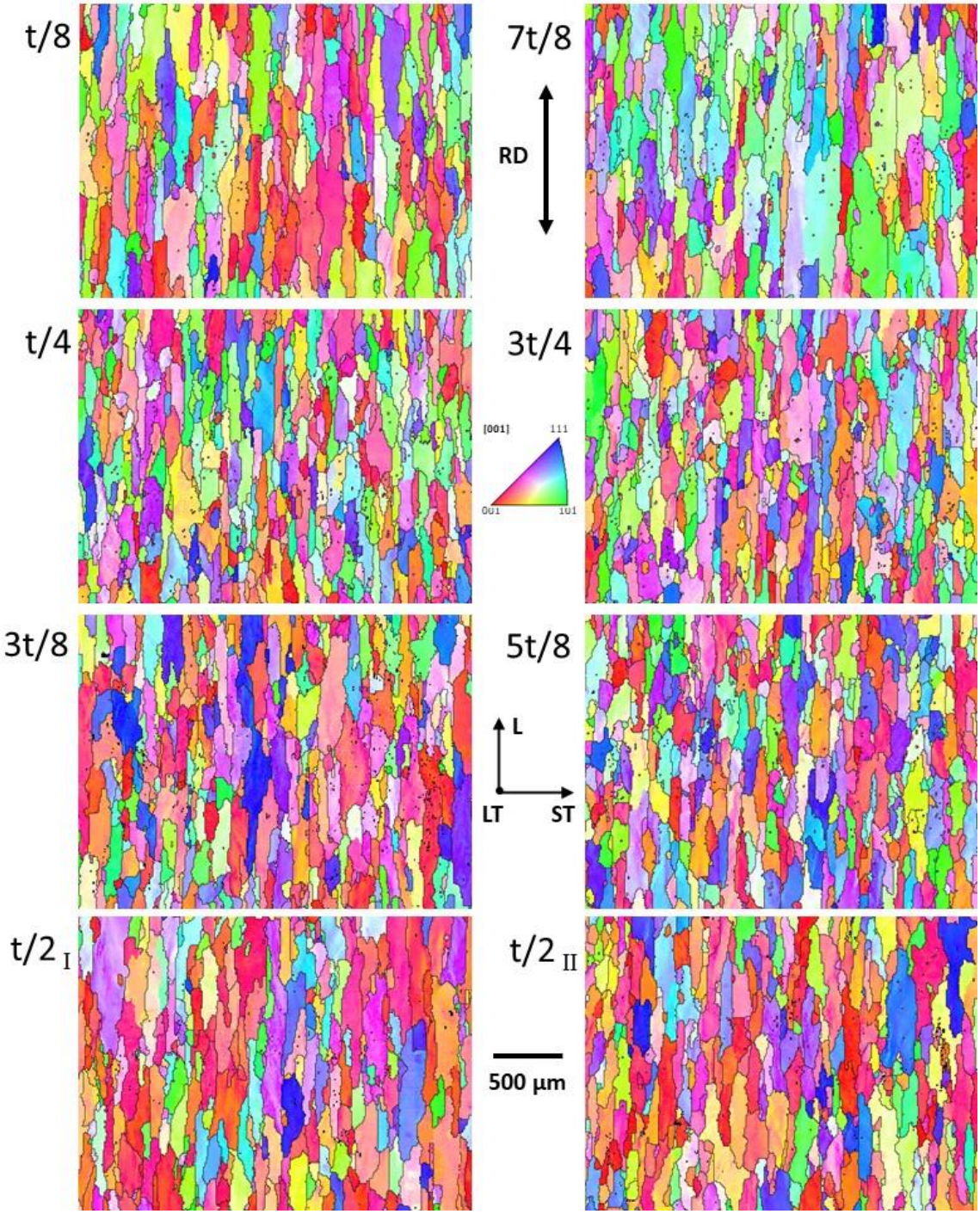

Figure 2. Full spectrum inverse pole figure maps, with ND as the reference orientation, (IPF_{ND}) of the L-ST plane at the selected through-thickness locations in the plate.

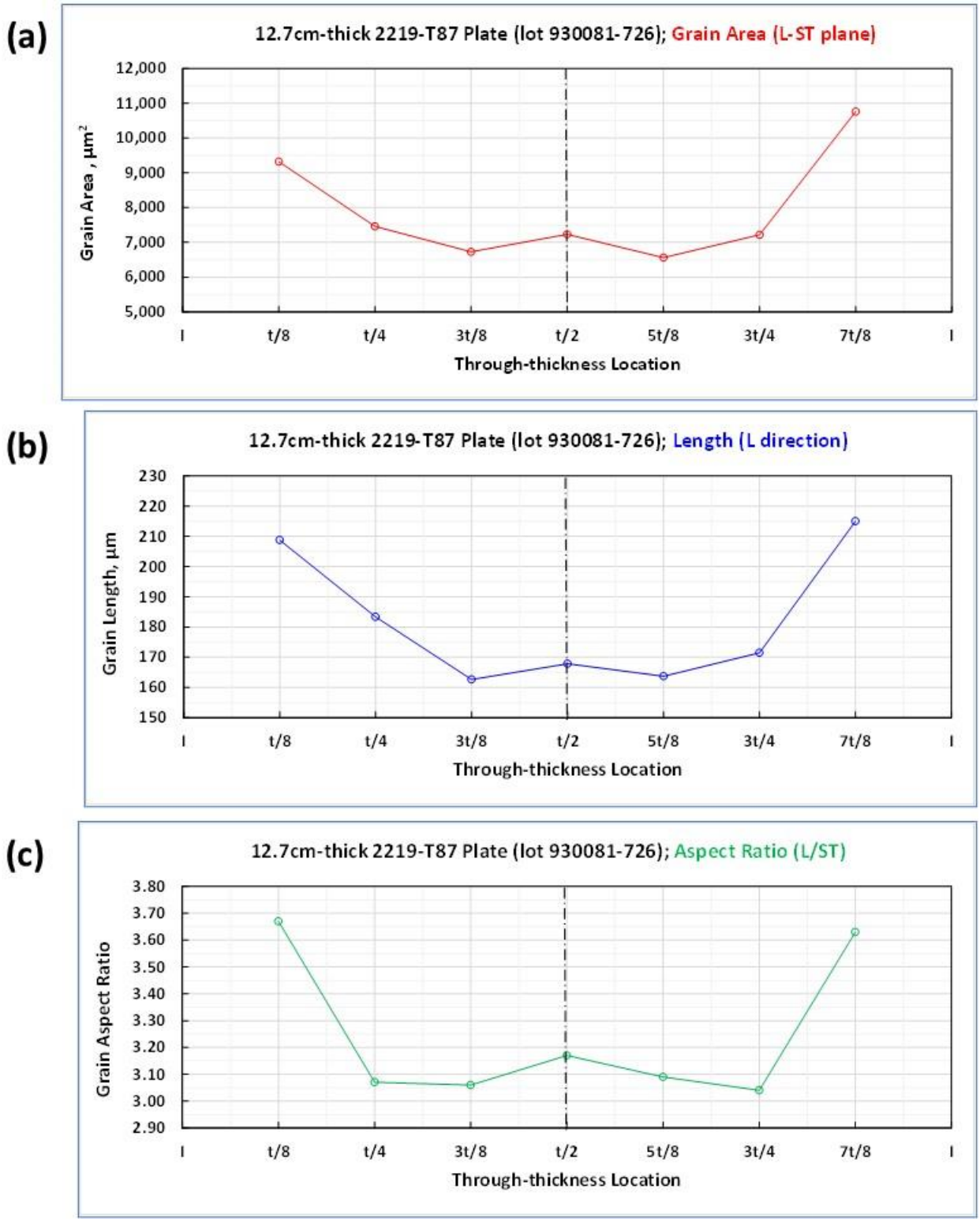

Figure 3. Data illustrating average grain size and morphology on the L-ST plane as a function of through-thickness location: (a), grain area; (b), grain length, $\overline{g}_L$; (c), aspect ratio, $\overline{g}_L$ / $\overline{g}_{ST}$.

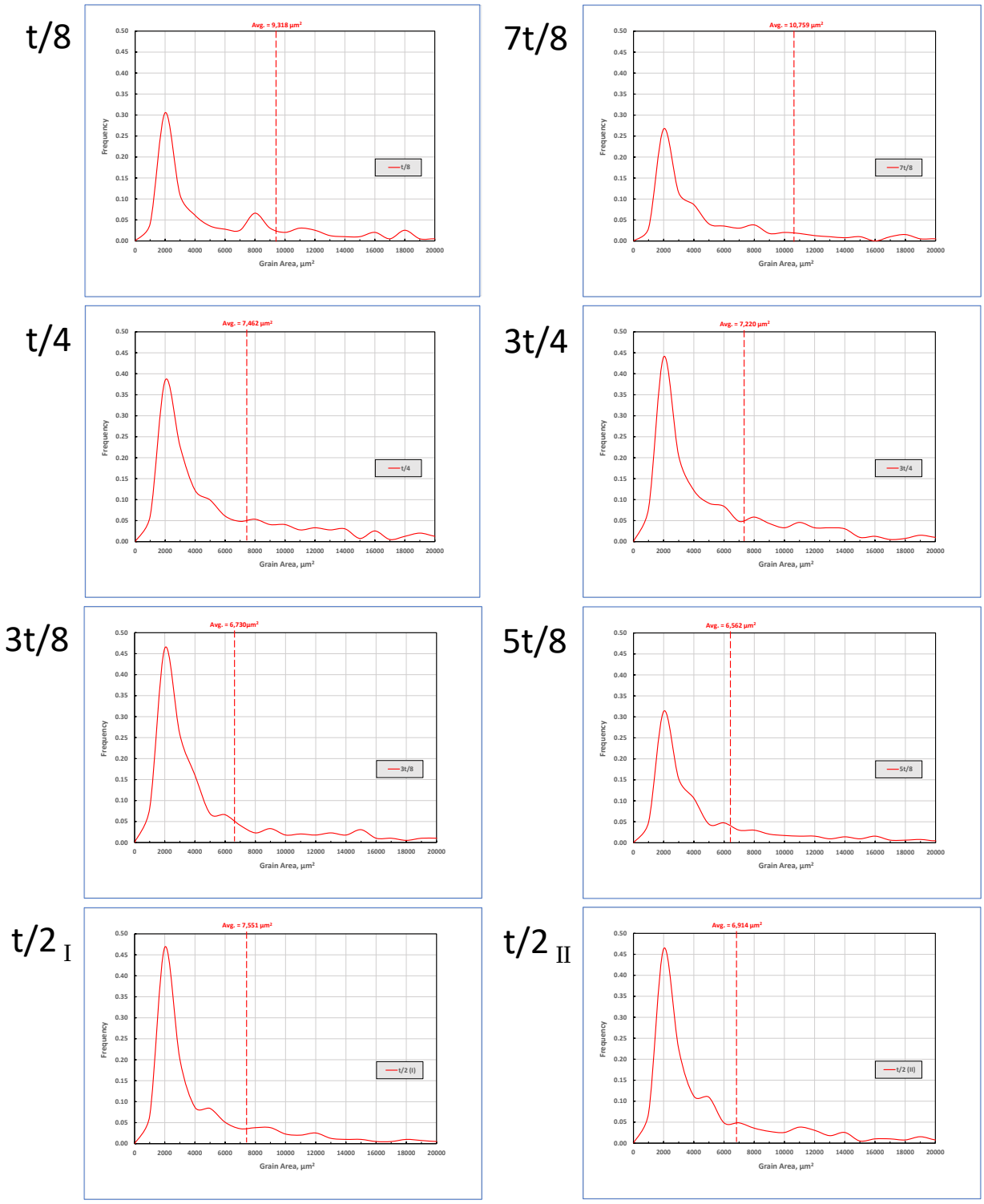

Figure 4. Grain area distribution plots at the various through-thickness locations on the L-ST plane of the plate. The purpose is to verify that the distribution of grain area is not bimodal and instill confidence in the average values reported.

Table 5. ODF analysis at the through-thickness locations: area fractions of selected grain orientations, with recognized components divided into rolling, shear and RX categories.

Texture Components		Area Fraction @ Through-Thickness Location						
		t/8	t/4	3t/8	t/2	5t/8	3t/4	7t/8
ROLLING	Bs	0.032	0.024	0.018	0.014	0.022	0.031	0.041
	S	0.014	0.019	0.010	0.016	0.037	0.023	0.065
	S'_1	0.008	0.022	0.030	0.011	0.011	0.042	0.031
	S'_2	0.058	0.076	0.046	0.038	0.043	0.031	0.119
	Cu	0.039	0.026	0.022	0.012	0.032	0.047	0.048
	Total	*0.151*	*0.167*	*0.126*	*0.090*	*0.138*	*0.168*	*0.301*
SHEAR	X_R	0.020	0.028	0.027	0.012	0.019	0.042	0.090
	E	0.017	0.014	0.051	0.044	0.048	0.015	0.020
	F	0.043	0.065	0.080	0.055	0.089	0.062	0.051
	H	0.019	0.001	0.032	0.019	0.019	0.009	0.018
	I	0.022	0.043	0.073	0.067	0.090	0.048	0.047
	Total	*0.121*	*0.151*	*0.263*	*0.196*	*0.265*	*0.176*	*0.226*
RECRYSTALLIZATION	Goss	0.019	0.016	0.008	0.013	0.006	0.016	0.009
	Cube	0.050	0.021	0.015	0.076	0.029	0.054	0.013
	RC_{RD1}	0.059	0.067	0.076	0.116	0.042	0.083	0.028
	RC_{RD2}	0.072	0.068	0.007	0.032	0.049	0.036	0.075
	RC_{ND1}	0.106	0.079	0.115	0.113	0.075	0.056	0.037
	RC_{ND2}	0.027	0.033	0.066	0.058	0.046	0.039	0.024
	P	0.054	0.065	0.045	0.013	0.047	0.065	0.038
	Q	0.158	0.141	0.110	0.141	0.141	0.122	0.084
	R	0.037	0.018	0.022	0.017	0.010	0.025	0.016
	Bs_{RX}	0.097	0.085	0.063	0.056	0.053	0.073	0.054
	Total	*0.679*	*0.593*	*0.527*	*0.633*	*0.494*	*0.568*	*0.378*
OTHERS		0.049	0.089	0.084	0.081	0.103	0.088	0.095

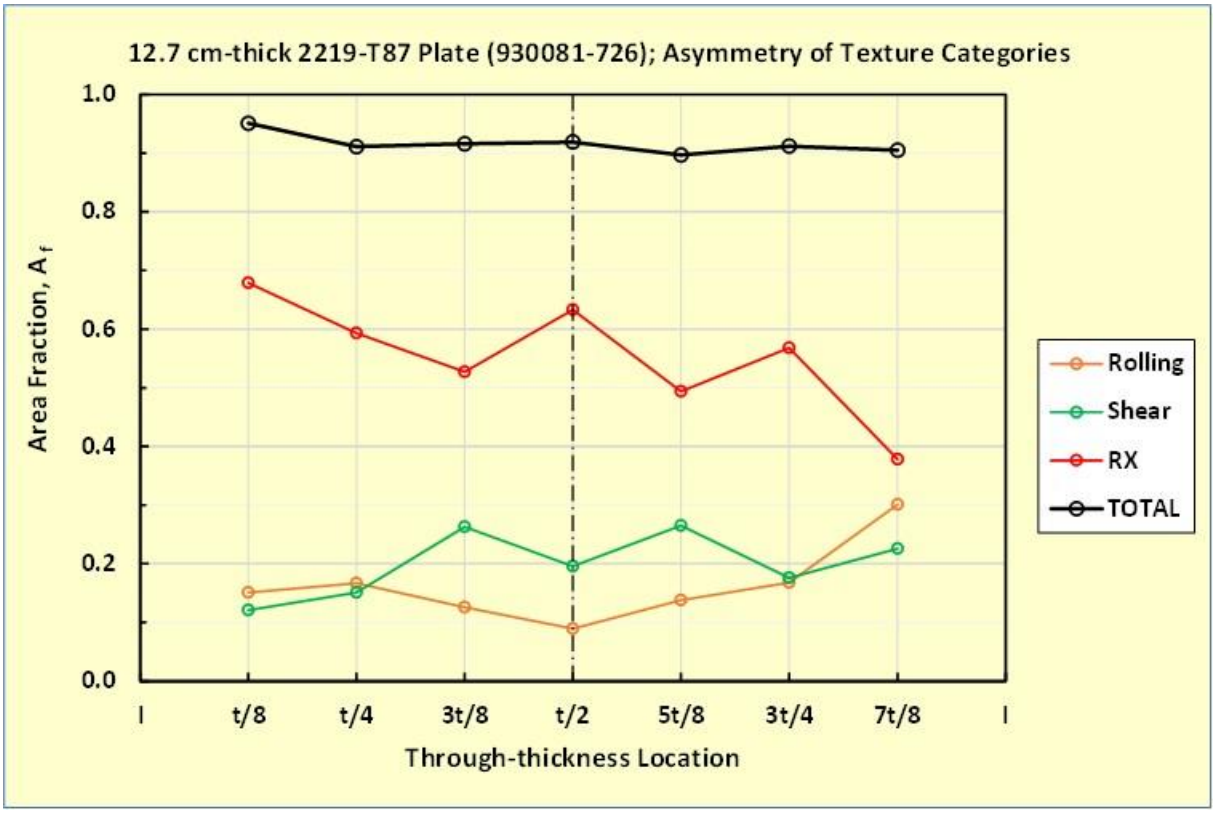

Figure 5. Area fractions of the rolling, shear and RX texture categories as a function of through-thickness location. The 'total' category reveals that the analysis accounts for A_f > 90% of the textural composition in the plate cross-section.

Table 6. Isolated area fractions of the rolling, shear and RX categories at the t/8, t/2, and 7t/8 locations. The general trend comprises decreasing RX, with slightly increasing shear, and rolling through the plate cross-section.

Texture Category	Area Fraction, %		
	t/8	t/2	7t/8
RX	67.9	63.3	37.8
Shear	12.1	13.9	22.6
Rolling	15.1	9.0	30.1
Total	*95.1*	*91.8*	*90.5*

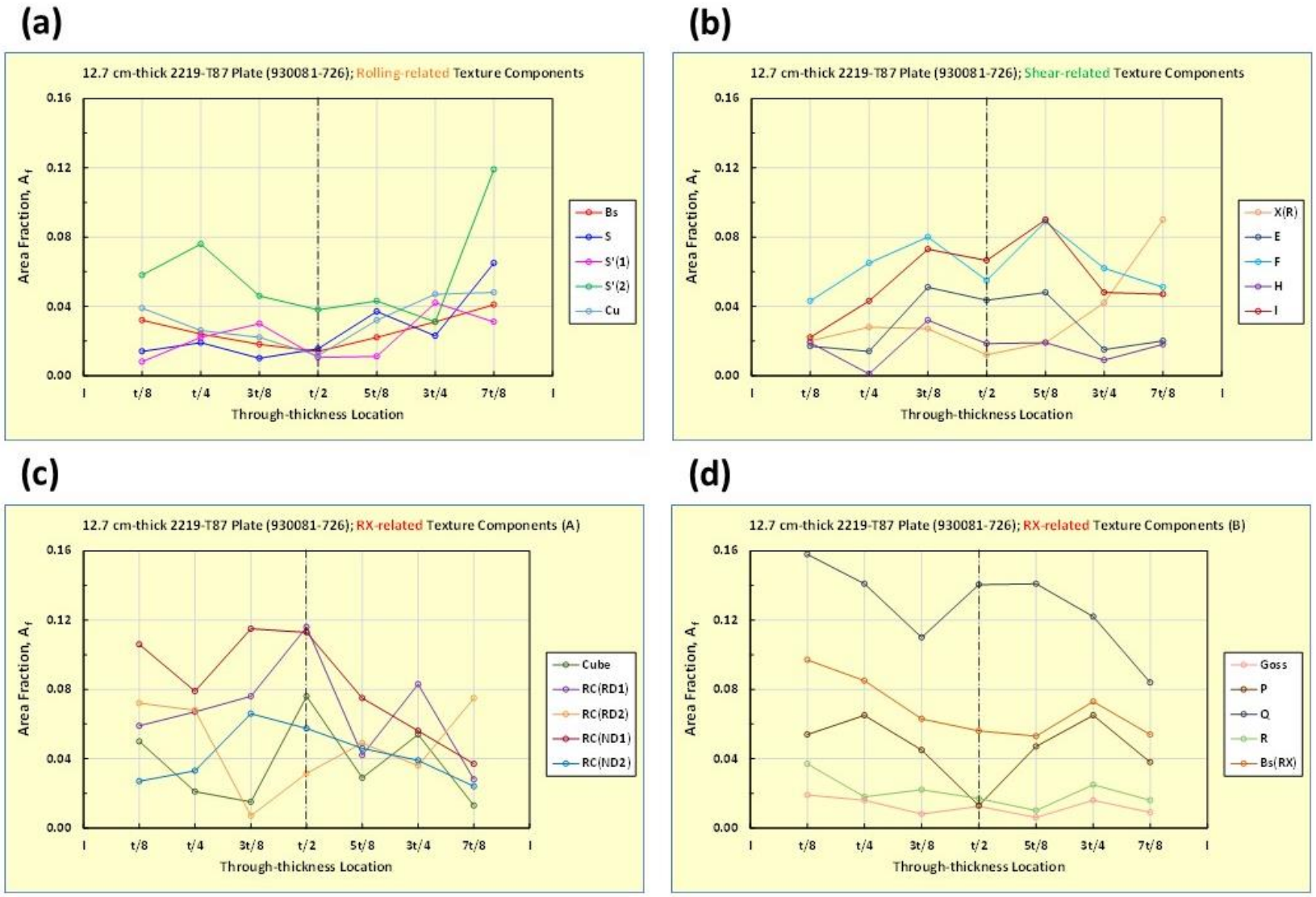

Figure 6. Area fractions of individual components as a function of through-thickness location; (a) rolling-related β-fiber; (b) shear-related {hkl}<110>; (c) ***Cube***-related {001}<uvw> and {hkl}<100>; (d) PSN-related orientations.

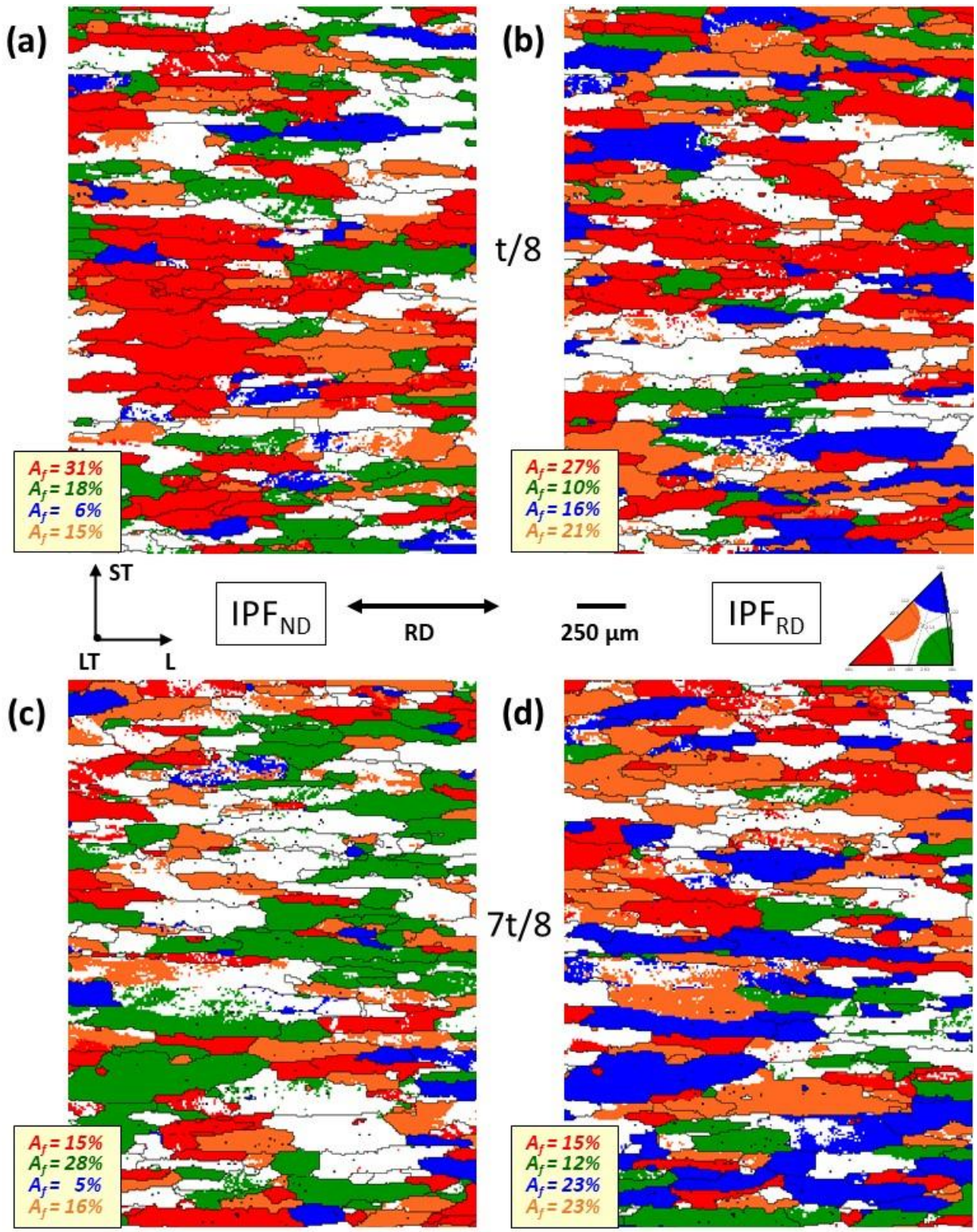

Figure 7. Distilled IPF_{ND} and IPF_{RD} maps revealing the areal fraction and spatial distribution of <100>-, <110>-, <111>-, and <112>-fibers: (a) & (b), at the t/8 location; (c) & (d), at the 7t/8 location.

3.2 Microtexture Related to Fracture Locations

The second objective of the EBSD analysis was to evaluate differences in grain orientation and distribution that could influence ST ductility at the common fracture locations (3t/8, t/2, or 5t/8). The distilled IPF_{ND} maps in Figure 8 indicate that the areal fractions of the four fibers are similar at 3t/8 and 5t/8, average values comprising $\bar{A}_f$ = 32%, 12%, 14%, and 18%. The fractions are also similar at $t/2_I$ and $t/2_{II}$, average values comprising $\bar{A}_f$ = 44%, 8%, 9%, and 14%. The largest difference between the two pairs of locations involves the dominant RX category components that are mostly contained within the <001> and <011> fibers. The {hkl} data suggest that ***Cube***, $\boldsymbol{RC_{RD1}}$, $\boldsymbol{RC_{ND1}}$, $\boldsymbol{RC_{ND2}}$, and/or ***Q*** oriented grains may be more prevalent at t/2 than either 3t/8 or 5t/8. The data may also indicate that grains with ***Goss***, $\boldsymbol{RC_{RD2}}$, and/or ***P*** orientations may be less prevalent at t/2 than either 3t/8 or 5t/8. The {hkl} data for the shear category components, contained in the <111> and <112> fibers, suggest a comparable decrease in ***E***, ***F***, and/or ***I*** oriented grains. The data for the rolling category components, contained in the <011> and <112> fibers, may also indicate a marginal decrease in ***Bs*** and/or ***Cu*** oriented grains.

The distilled IPF_{RD} maps in Figure 9 show that the areal fractions of the four fibers are similar at 3t/8 and 5t/8, average values comprising $\bar{A}_f$ = 18%, 24%, 9%, and 20%. The fractions are also similar at $t/2_I$ and $t/2_{II}$, average values comprising $\bar{A}_f$ = 30%, 20%, 6%, and 20%. Again, the largest change concerns the dominant RX category components that are mostly contained within the <100> fiber. The <uvw> data suggest that ***Goss***, ***Cube***, $\boldsymbol{RC_{RD1}}$, $\boldsymbol{RC_{RD2}}$ and/or $\boldsymbol{RC_{ND1}}$ oriented grains may be more prevalent at t/2 than either 3t/8 or 5t/8. The data also suggest that grains with $\boldsymbol{RC_{ND2}}$ and/or ***P*** orientations may be marginally less prevalent at t/2 than either 3t/8 or 5t/8. The <uvw> data for the shear category components, mostly contained in the <110> fiber, indicate a comparable decrease in ***E***, ***H***, and/or ***I*** oriented grains. The data for the rolling category components, mostly contained in the <211> fiber, suggest no change in the significant areal fraction of ***Bs***, ***S***, $\boldsymbol{S'_1}$ and/or $\boldsymbol{S'_2}$ oriented grains.

The third objective of the EBSD analysis was to evaluate differences in misorientations and structures of GBs intersecting the L-ST plane that could influence intergranular fracture. The MDF plots in Figure 10 show the population of GB misorientations at 3t/8, 5t/8, $t/2_I$, and $t/2_{II}$, each compared with the theoretical random distribution. The positions of CSL boundaries with rotation angles between 15° and 65° (Table 4) are also included for correlations. Although unlikely to be statistically significant, there are subtle differences between the measured and theoretical distribution of GB misorientations. At each of the locations, no discernible pattern in the positive and negative displacements emerges. However, comparing the common fracture locations (3t/8 or 5t/8 versus $t/2_I$, or $t/2_{II}$) does reveal separations of similar magnitude. Consequently, GBs at the 3t/8 and $t/2_{II}$ locations that deviated above and below random the most (shaded areas) were selected for closer scrutiny.

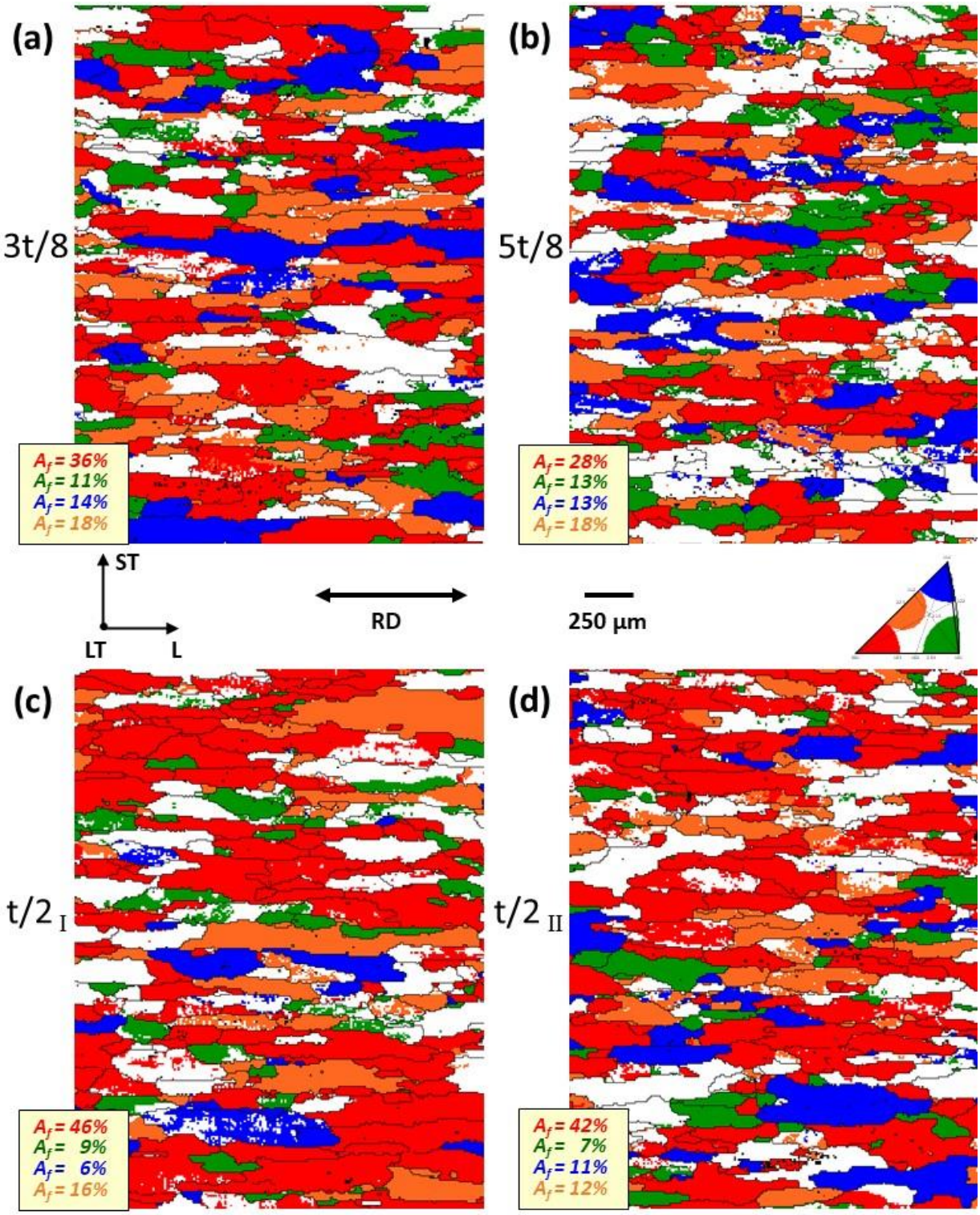

Figure 8. Distilled IPF_{ND} maps revealing the areal fraction and spatial distribution of <001>-, <011>-, <111>-, and <112>-fibers at locations: (a), 3t/8; (b), 5t/8; (c), $t/2_I$; (d), $t/2_{II}$. Averages comprise $\bar{A}_f$ = 32%, 12%, 14%, 18% at 3t/8 + 5t/8, and $\bar{A}_f$ = 44%, 8%, 9%, 14% at t/2I + $t/2_{II}$.

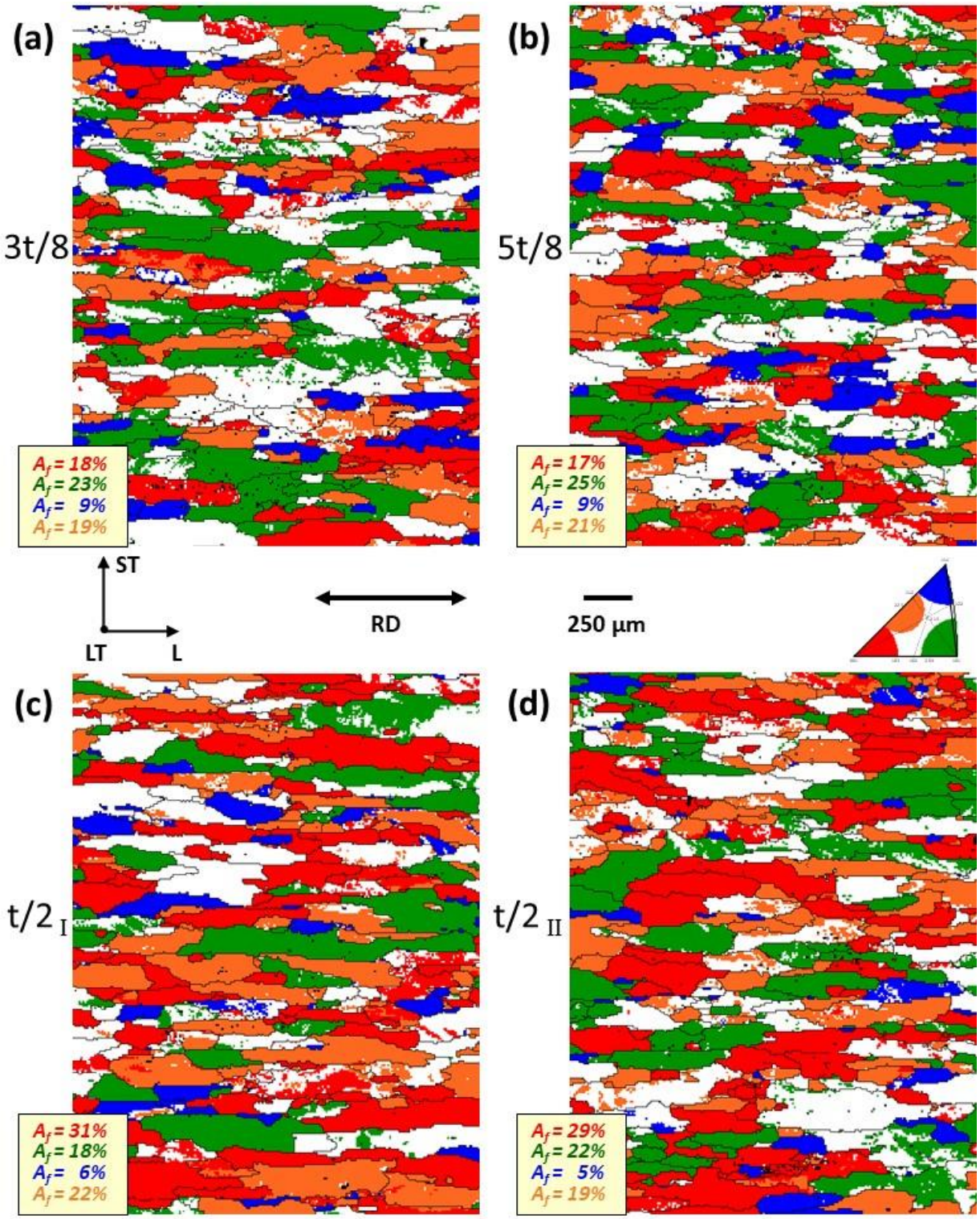

Figure 9. Distilled IPF_{RD} maps revealing the areal fraction and spatial distribution of <100>-, <110>-, <111>-, and <211>-fibers at locations: (a), 3t/8; (b), 5t/8; (c), $t/2_I$; (d), $t/2_{II}$. Averages comprise $\bar{A}_f$ = 18%, 24%, 9%, 20% at 3t/8 + 5t/8, and $\bar{A}_f$ = 30%, 20%, 6%, 20% at $t/2_I$ + $t/2_{II}$.

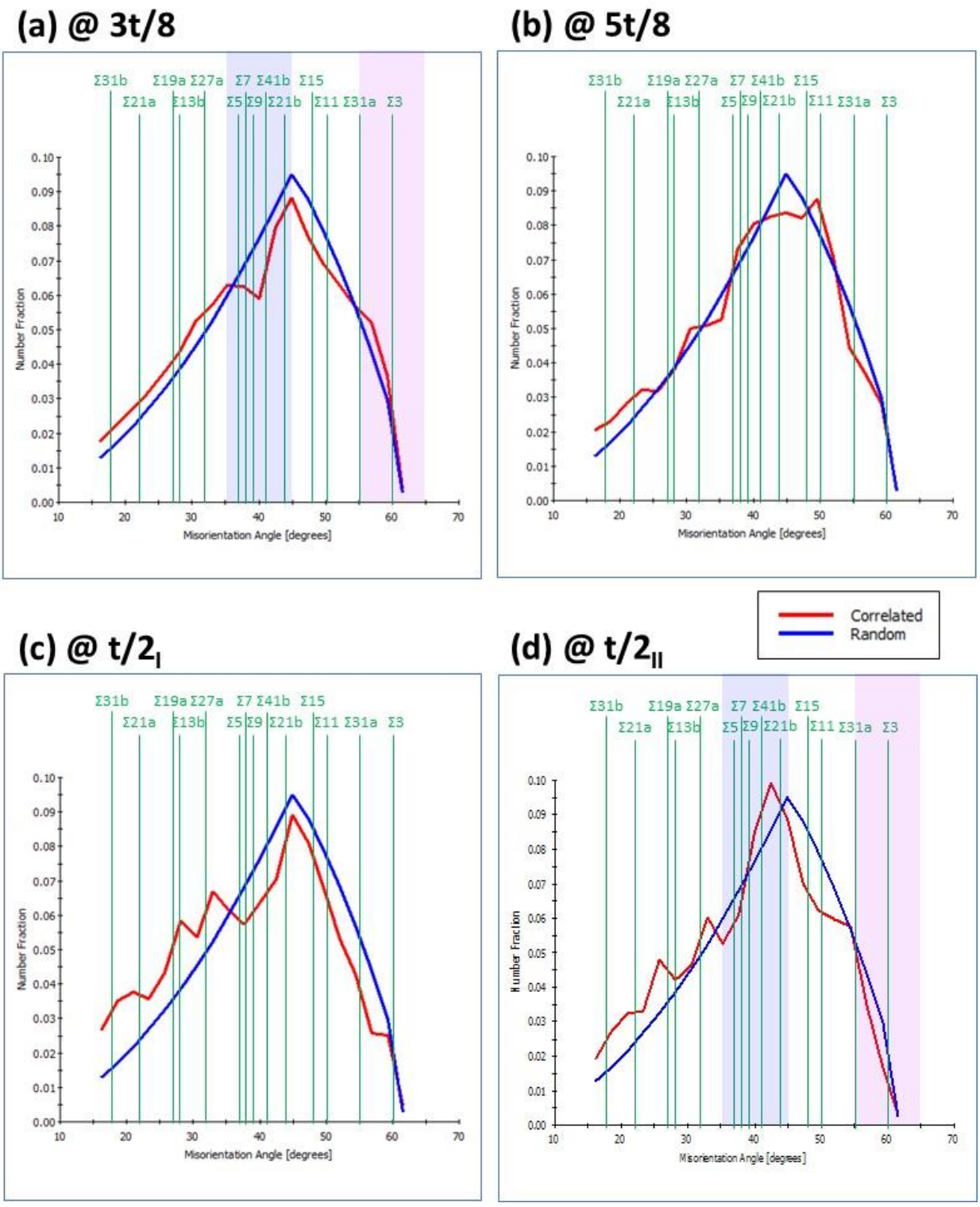

Figure 10. Misorientation distribution function (MDF) plots comparing: (a), 3t/8; (b), 5t/8; (c), $t/2_I$; (d), $t/2_{II}$ locations. GB misorientations (---) are related to the theoretical random distribution (---) and the angular positions of CSL boundaries (---) are included (Table 2).

In addition to the misorientation distribution, considering the spatial distribution of GB characteristics may provide some insight on fracture behavior. The 'GB misorientation maps' in Figure 11 allow the length fractions and distributions of GBs at 3t/8 and t/2$_{II}$ to be compared. The data are presented for rotation angles between 15° and 65°, divided into 10° increments. The total length of GBs is 130 mm at 3t/8 and 129 mm at t/2$_{II}$, which is consistent with the grain size/morphology similarities. The most significant difference is the length fractions of GBs with rotation angles between 35-45° and 55-65°. At 3t/8, L_f = 28.5 % for the 35-45° range and L_f = 11.0 % for the 55-65° range (of the 130 mm). At t/2$_{II}$, L_f = 32.7 % for the 35-45° range and L_f = 6.6 % for the 55-65° range (of the 129 mm).

Complementary to the misorientation and spatial distributions, evaluation of the density and distribution of CSL-type boundaries may provide some additional insight on fracture behavior. The 'CSL boundary maps' in Figure 12 permit the structure of the constituent GBs at 3t/8 and t/2$_{II}$ to be compared. The total length of all CSLs is 11.9 mm at 3t/8 and 12.3 mm at t/2$_{II}$, which represents ≈ 9 % of the total GB length in both instances. The total length of low index CSLs, Σ3, Σ5, Σ7, and Σ9, is 6.3 mm at 3t/8 and 6.6 mm at t/2$_{II}$, which represents ≈ 5 % of the total GB length in both cases. The most significant difference is the change in length fractions of Σ5 and Σ9 CSL boundaries, with 37°∧<100> and 39°∧<110> misorientations. At 3t/8, L_f = 12.6 % for the Σ5's and L_f = 45.4 % for the Σ9's (of the 6.3 mm). At t/2$_{II}$, L_f = 25.7 % for the Σ5's and L_f = 36.6 % for the Σ9's (of the 6.6 mm). There is also a decrease in the length fractions of Σ3 and Σ7 boundaries, with 60°∧<111> and 38°∧<111> misorientations. At 3t/8, L_f = 17.4 % for the Σ3's and L_f = 24.6 % for the Σ7's (of the 6.3 mm). At t/2$_{II}$, L_f = 15.9 % for the Σ3's and L_f = 21.8 % for the Σ7's (of the 6.6 mm).

4.0 Discussion

4.1 Through-thickness Microtextural Asymmetry

In Al alloy rolled product, the REX texture exhibits a crystallographic relationship with the prior DEF texture, which leads to new grains assuming specific orientations. RX orientations nucleate at inhomogeneities in the deformed grain structure, such as ***Cube***, ***RC$_{RD}$***, and ***P*** at transition bands, or ***Q*** at shear bands [ref. 15]. The relative area fractions of these components tend to be dependent on rolling parameters, such as total strain and temperature. PSN-related orientations, such as ***RC$_{ND}$***, ***P***, and ***Q***, originate within localized deformation zones that are more dependent on both the size and distribution of second phase particles. The ***RC$_{ND}$*** and ***P*** components are most frequently associated with PSN in recrystallized Al alloys [ref. 16]. The ***Q*** component may be uncommon in many Al alloys [ref. 30], but a lack of shear bands may be compensated by an abundance of coarse particles in high-solute Al 2219.

Consequently, searching for relationships between other texture components or microstructural characteristics and variations in area fractions of PSN components represents a prudent strategy. The plot in Figure 13 isolates the contributions of PSN components to the microtexture asymmetry through the plate cross-section. Generally, the area fractions of the top four components, ***Q***, ***RC$_{ND1}$***, ***RC$_{RD1}$***, and ***Cube***, trend downwards from t/8 to 7t/8. The cross-sectional profile of each exhibits marked discontinuities at the common fracture locations, i.e. 3t/8 (or 5t/8) and t/2. The variations comprise a valley at 3t/8 for ***Q*** and ***Cube***, a peak at t/2 for ***RC$_{ND1}$***, ***RC$_{RD1}$***, and ***Cube***, plus a valley at 5t/8 for ***RC$_{RD1}$*** and ***Cube***.

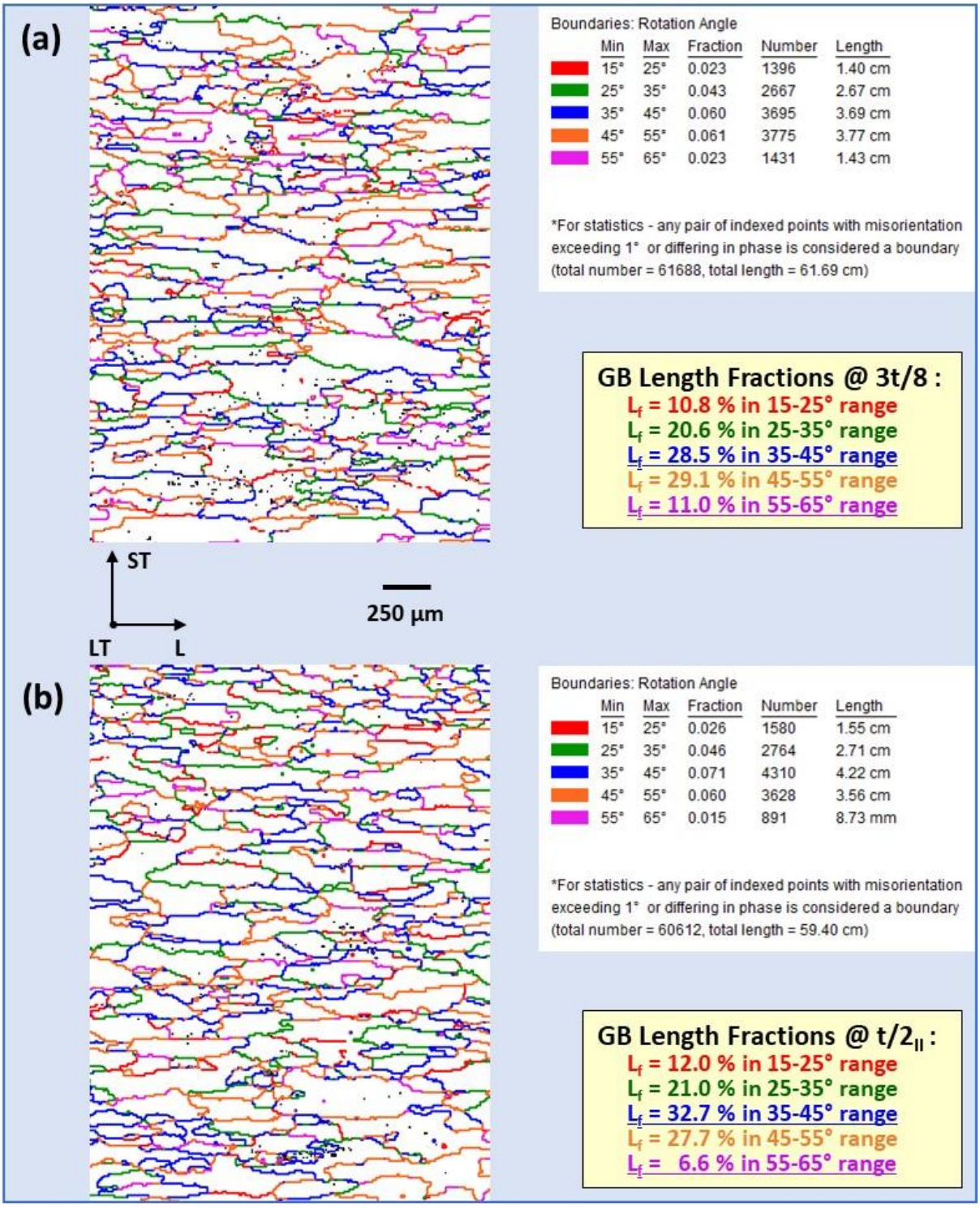

Figure 11. Data showing the spatial distribution and composition of GB misorientations: (a), at 3t/8; (b), at $t/2_{II}$. The largest differences between the locations are the length fractions of GBs within the 35°- 45° and 55°- 65° angular increments.

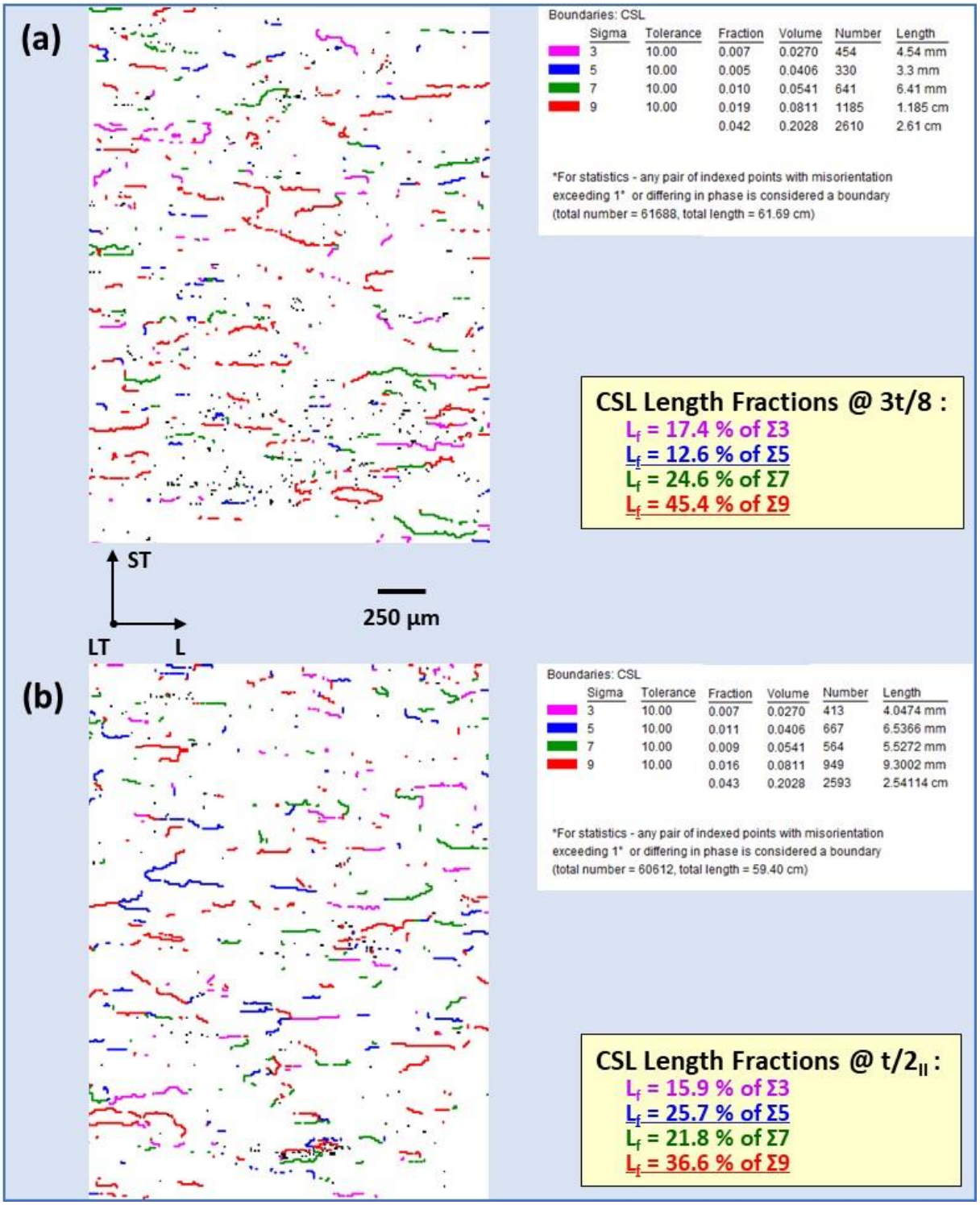

Figure 12. Data showing the spatial distribution and composition of low index CSL boundaries: (a), at 3t/8; (b), at $t/2_{II}$. The largest differences between the locations are the length fractions of Σ5 and Σ9 CSLs.

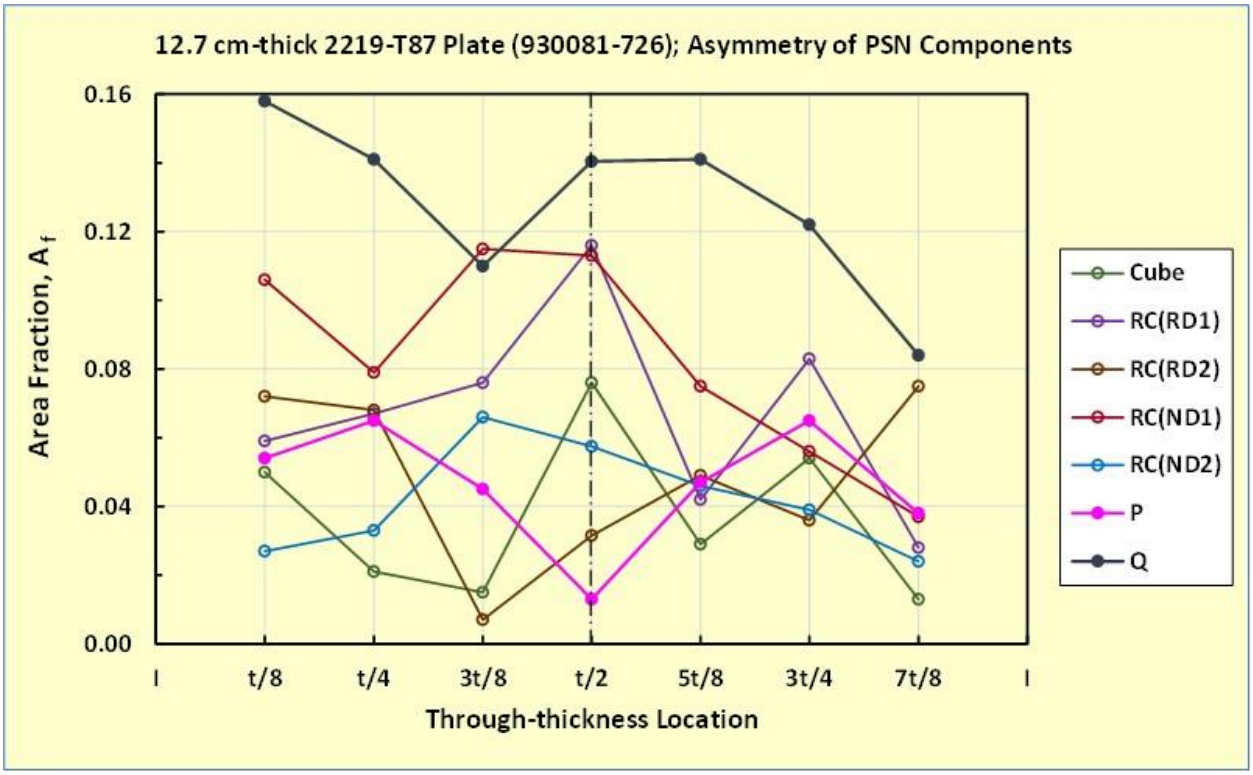

Figure 13. Isolation of the contributions of PSN components to the microtexture asymmetry through the plate cross-section. In contrast with ***Q*** and other profiles, ***P*** is the only component that exhibits a through-thickness variation that is almost symmetrical about the mid-plane.

A comparison between the cross-sectional asymmetry of DEF components, t/8 and 7t/8 in Figures 6(a)&(b), reveals the following correlations. The top four DEF components are the shear-related ***I***, ***F***, and ***E***, plus the rolling-related $\boldsymbol{S'_2}$. The cross-rolling-related $\boldsymbol{X_R}$ is also notable because the area fraction is much higher at 7t/8 than the rest of the cross-section. The downward trend in ***Q***, $\boldsymbol{RC_{ND1}}$, $\boldsymbol{RC_{RD1}}$, and ***Cube*** is countered by an upward trend in ***I***, ***F***, and $\boldsymbol{X_R}$ from t/8 to 7t/8. The symmetrical ***E*** component is low at t/8 and 7t/8, higher at 3t/8, t/2, and 5t/8, but still below ***I*** and ***F***. The cross rolling-related $\boldsymbol{X_R}$ component is notable because the area fraction is much higher at 7t/8 than the majority of the cross-section. The profile of $\boldsymbol{X_R}$ displays a minimum at t/2 and a maximum at 7t/8.

A similar comparison with the DEF components at fracture locations, 3t/8, t/2, and 5t/8 in Figures 6(a)&(b), reveals the following correlations. Again, the top four DEF components are the shear-related ***I***, ***F***, and ***E***, plus the rolling-related $\boldsymbol{S'_2}$. The valley at 3t/8 for ***Q*** and ***Cube*** coincides with a peak for ***F***, ***I***, and ***E***. The peak at t/2 for $\boldsymbol{RC_{ND1}}$, $\boldsymbol{RC_{RD1}}$, and ***Cube*** coincides with a valley for ***I***, ***F*** and ***E*** (plus a minimum for $\boldsymbol{X_R}$). The valley at 5t/8 for $\boldsymbol{RC_{RD1}}$ and ***Cube*** coincides with a peak for ***F***, ***I***, and ***E***. The rolling-related $\boldsymbol{S'_2}$ component is also notable because the area fraction is much higher at 7t/8 than the majority of the cross-section. The profile of $\boldsymbol{S'_2}$ displays a minimum at 3t/4 and a maximum at 7t/8. The area fraction of $\boldsymbol{S'_2}$ shows an intermediate peak at t/4 and is intermediate at 3t/8, t/2, and 5t/8.

4.2 Through-thickness Microstructural Variations

A comparison with the cross-sectional variations in grain size, t/8 and 7t/8 in Figure 3(a), reveals the following correlations. The area of elongated grains adjacent to the plate surfaces is higher, t/8 ≈ 22 % and 7t/8 ≈ 36 %, than in the central cross-section. Note that the number of partial grains omitted from the analysis (cut-off by the perimeter of the sampling area) increases with grain length. Therefore, the higher values for grain area reported for the t/8 and 7t/8 locations are probably conservative. The area fractions of ***Q***, $\boldsymbol{RC_{ND1}}$, $\boldsymbol{RC_{RD1}}$, and ***Cube*** exhibit the steepest gradients (increasing or decreasing) in the same regions. The higher grain sizes coincide with ***Q*** exhibiting a maximum at t/8 and a minimum at 7t/8. The $\boldsymbol{X_R}$, and ***I*** components both show minima at the t/8 location. In contrast, the $\boldsymbol{X_R}$, and $\boldsymbol{S'_2}$ components both show maxima at the 7t/8 location. The lower grain sizes around the mid-plane coincide with $\boldsymbol{RC_{RD1}}$ and ***Cube*** reaching maxima, and ***P*** exhibiting a minimum at t/2.

A comparison with the distribution of GB misorientations and CSL boundaries at fracture locations, represented by 3t/8 and $t/2_{II}$, reveals the following correlations. The data for the 3t/8 location in Figure 11(a) and Table 7(a) indicate that the total length of CSLs represents 9.2 % of the total length of GBs. The length fractions of GBs with misorientations within the intermediate angular ranges (35°- 45° and 45°- 55°) are equally prevalent. The data for the 3t/8 location in Figure 12(a) and Table 7(b) indicate that the combined length of low index CSLs (Σ3, Σ5, Σ7, Σ9) represents only 4.9 % of the total GB length at the 3t/8 location. The length fraction of Σ9, followed by Σ7, are the most prevalent among the low index CSL boundaries. These CSLs both fall within the 35°- 45° angular increment of GB misorientations (Σ9; 39°∧<110> and Σ7; 38°∧<111>).

Table 7. A comparison of the GB characteristics at the 3t/8 and $t/2_{II}$ locations: (a), GB misorientations; (b), low index CSL boundaries. GBs misoriented in the 35° to 45° range are most prominent, and Σ9 CSLs are most prevalent within that angular increment.

(a)

Grain Boundary Misorientation	Length Fraction, %	
	3t/8	$t/2_{II}$
15°-25° range	10.8	12.0
25°-35° range	20.6	21.0
35°-45° range	**28.5**	**32.7**
45°-55° range	29.1	27.7
55°-65° range	11.0	6.6

(b)

Low Index CSL Boundary	Length Fraction, %	
	3t/8	$t/2_{II}$
Σ3; 60°^<111>	17.4	15.9
Σ5; 37°^<100>	12.6	25.7
Σ7; 38°^<111>	24.6	21.8
Σ9; 39°^<110>	**45.4**	**36.6**

The data for the $t/2_{II}$ location in Figure 11(b) and Table 7(a) indicate that the total length of CSLs represents 9.5 % of the total length of GBs. The length fractions of GBs with misorientations within the intermediate angular ranges (35°- 45° and 45°- 55°) are the most prevalent. The data for the $t/2_{II}$ location in Figure 12(b) and Table 7(b) indicate that the combined length of low index CSLs (Σ3, Σ5, Σ7, and Σ9) represents only 5.1 % of the total GB length at the 3t/8 location. The length fraction of Σ9, followed by Σ7, are the most prevalent among the low index CSL boundaries. These CSLs both fall within the 35°- 45° angular increment of GB misorientations (Σ9; 39°∧<110> and Σ7; 38°∧<111>).

In order to assess any further relationships between textural and microstructural characteristics, the plots in Figure 14 were extracted from a sister study within the current investigation [data courtesy of Medders]. Although data for three lots are presented in Figure 14(b)&(c), attention is focused on lot 930082-723 (gray line) because it is common to all three plots. At ≈ 3t/8, note that there is a minimum in the Cu content profile that correlates with maxima in the profiles for the size and area fraction of θ-phase particles. A comparison with the typical cross-sectional variations in Cu content presented in Figure 14(a) reveals the following correlations. The average Cu content in the plate cross-section is ≈ 6.4 wt.%, but slowly decreases from ≈ 6.6 wt.% at t/8, to ≈ 6.3 wt.% at 3t/8, and then quickly decreases to ≈ 5.9 wt.% at t/2.

P is the only PSN component that shows a roughly symmetrical variation in area fraction ($\overline{A}_f$ = 4.6% at t/8, $\overline{A}_f$ = 4.6% at 3t/8, and $\overline{A}_f$ = 1.3% at t/2) through the cross-section. Although the least prominent, the through-thickness trend in ***P*** appears to track with the Cu macro-segregation profile. The minimum in Cu content at t/2 does coincide with maxima for the ***RC$_{RD1}$***, ***RC$_{ND1}$***, and ***Cube*** components. The intermediate Cu content at 3t/8 may coincide with either a minimum (3t/8), or a maximum (5t/8) in ***Q***. The ***Cube*** component does exhibit a minimum at both 3t/8 and 5t/8. Interestingly, the maximum in Cu content at t/8 may coincide with either the maximum (t/8) or the minimum (7t/8) for the most prominent ***Q*** component.

A comparison with the typical cross-sectional variations in θ-phase particle size presented in Figure 14(b) reveals the following correlations. The average size of θ-phase particles is 10 μm^2 at t/6 ($\overline{d}_P \approx 3.6$ μm), 24 μm^2 at 3t/8 ($\overline{d}_P \approx 5.5$ μm), and 7 μm^2 at t/2 ($\overline{d}_P \approx 3.0$ μm) in lot 930082-723 that exhibits low ST ductility. The intermediate particle size at t/6 approximately coincides with either the maximum (t/8) or the minimum (7t/8) for the prominent ***Q*** component. The maximum particle size at 3t/8 may coincide with either a low (3t/8), or a high (5t/8) in ***Q***. The ***Cube*** component does exhibit a low at both 3t/8 and 5t/8. The minimum particle size at t/2 does coincide with maxima for the ***RC$_{RD1}$***, ***RC$_{ND1}$***, and ***Cube*** components.

A comparison with the typical cross-sectional variations in area fraction of θ-phase presented in Figure 14(c) reveals the following correlations. The average area fraction of the θ-phase is $\overline{A}_f \approx$ 1.4 % at t/6, $\overline{A}_f \approx$ 1.9 % at 3t/8, and $\overline{A}_f \approx$ 0.8 % at t/2 in lot 930082-723 that exhibits low ST ductility. The intermediate area fraction at t/6 approximately coincides with either the maximum (t/8) or the minimum (7t/8) for the prominent ***Q*** component. The maximum area fraction at 3t/8 may coincide with either a low (3t/8), or a high (5t/8) in ***Q***. The ***Cube*** component does exhibit a low at both 3t/8 and 5t/8. The minimum area fraction at t/2 does coincide with highs for the ***RC$_{RD1}$***, ***RC$_{ND1}$***, and ***Cube*** components.

In order to facilitate understanding, the through-thickness trends in area fraction and diameter of θ-phase particles are correlated with location-dependent variations in the dominant PSN components in Table 8. The symmetrical variations in particle size/distribution are probably related to casting practices, whereas the asymmetrical trends in microtexture/RX grain structure are more likely related to rolling procedures.

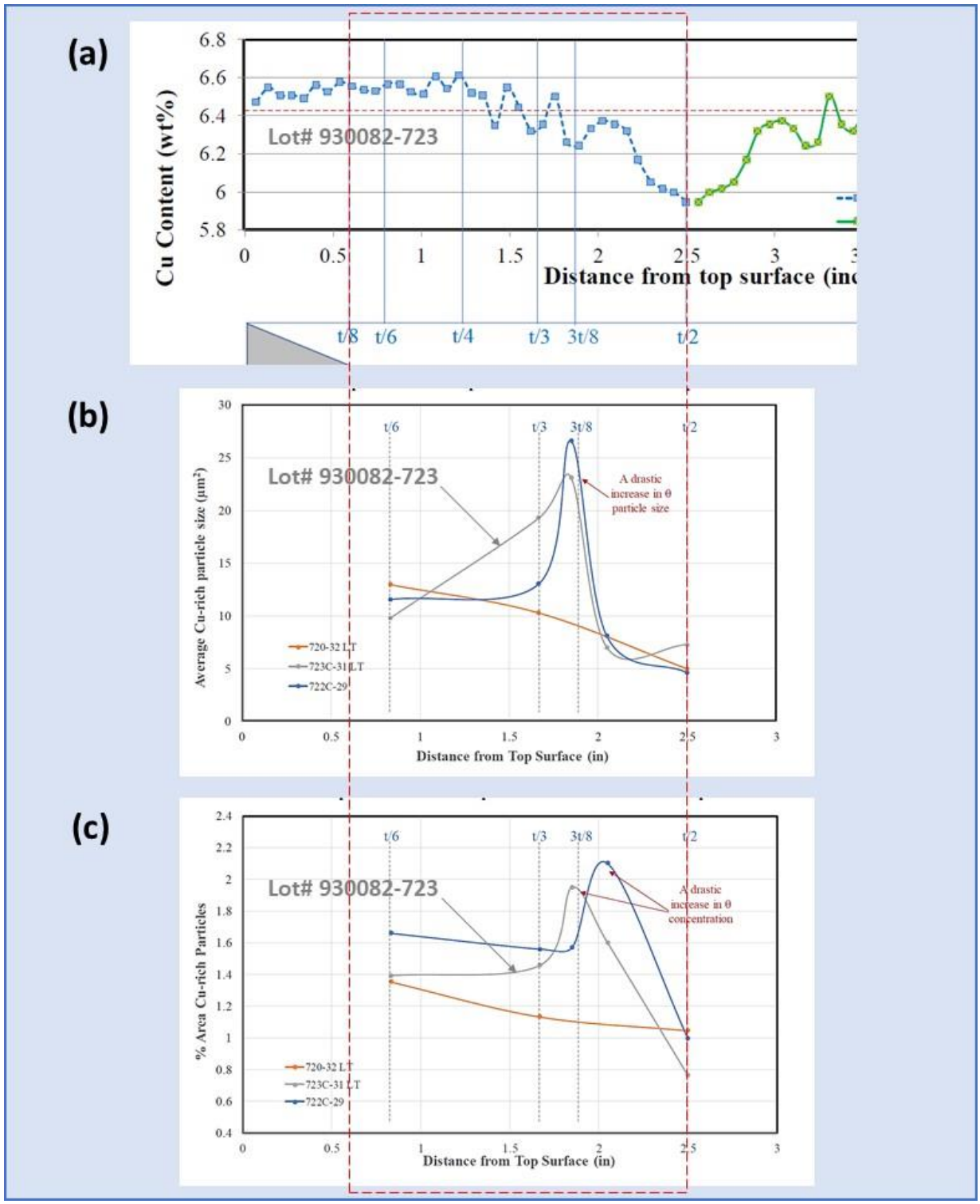

Figure 14. A comparison for 12.7-cm-thick 2219-T87 plate (lot 930082-723) of the cross-sectional variations in (a), Cu content; (b) θ-phase particle size; (c) area fraction of θ-phase [data courtesy of Medders].

Table 8. Average area fraction and diameter of θ-phase particles compared with dominant PSN components. Correlation of variations through the plate thickness (assuming cross-sectional symmetry for θ-phase attributes).

Al_2Cu θ-phase			PSN RX Components, A_f (%)				
Location	A_f, %	d_p, µm	Location	Q	Cube	RC_{RD1}	RC_{ND1}
t/6	1.4	3.6	t/8	15.8	5.0	5.9	10.6
3t/8	1.9	5.5	3t/8	11.0	1.5	7.6	11.5
t/2	0.8	3.0	t/2	14.1	7.6	11.6	11.3
3t/8	*1.9*	*5.5*	5t/8	14.1	2.9	4.2	7.5
t/6	*1.4*	*3.6*	7t/8	8.4	1.3	2.8	3.7

4.3 Microtextural Analyses Summary

In summary, the EBSD analyses clearly indicate that variations in the microtextural features through the plate cross-section are asymmetrical. The through-thickness perturbations in the composition and distribution of individual texture components are complex and vastly different. In general, decreases in the area fraction of DEF grains are countered by increases in the area fraction of REX grains. The shear-related and PSN-related components are far from symmetrical and tend to dominate the respective categories. Although ***Q*** is the strongest among PSN components, the 180° ambiguity in the data does not permit correlations with Cu content etc. ***Q*** does trend down (@ 3t/8), or up (@ 5t/8), that coincides with the brief surge in the size/area fraction of θ-phase particles at the same location(s). The ***P*** component is unique and exhibits a through-thickness trend that is almost symmetrical about the mid-plane (t/2). The cross-sectional gradients in ***P*** assume a profile that approximates the Cu macro-segregation profile in the plate and, thus, may be connected to fracture characteristics.

The differential in areal densities of the primary texture fibers between the mid-plane and the other locations may also have relevance to fracture behavior. The concurrent decrease in REX and increase in DEF grain orientations from t/2 towards 3t/8 or 5t/8 may increase mechanical anisotropy at the locations away from the mid-plane. As a consequence, strain localization at GBs may be accelerated and intergranular fracture could be promoted by these differences [ref. 18]. Comparing the GB characteristics is an exploratory exercise and drawing firm conclusions from the limited data analyzed is impractical.

The similarity between the total GB and CSL lengths at the common fracture locations (3t/8 to t/2) is striking and also confirms the comparable dimensions of the grain structures. GBs with intermediate misorientations are prominent 3t/8 to t/2 and the area fractions change slightly. Although less prominent, the area fraction of GBs with high misorientations decreases the most from 3t/8 to t/2. Σ9 and Σ7 CSLs are the most prevalent at 3t/8 and t/2, both within the intermediate misorientation range. Σ9; 39°∧<110> and Σ7; 38°∧<111> CSLs may be associated with shear grain orientations. The area fractions of Σ3, Σ7, and Σ9 CSLs decrease, and Σ5 CSLs increase, from 3t/8

to t/2. Similarly, Σ3; 60°∧<111> may also be shear-related, but Σ5; 37°∧<100> is associated with RX grain orientations.

Finally, the schematics in Figure 15 compare through-thickness variations in PSN component intensities, microstructural characteristics and ST ductility. Tensile elongation is *lower* when fracture occurs at the 3t/8 and 5t/8 locations (Figures 15(a)&(c)), where the local Cu content and areal fraction of θ-phase are *higher*. The areal fraction of the ***P*** component is *higher* and that of the $\boldsymbol{RC_{RD}}$ components is *lower*. In contrast, tensile elongation is *higher* when fracture occurs at the t/2 location (Figure 15(b)), where the local Cu content and areal fraction of θ-phase are *lower*. The areal fraction of the ***P*** component is *lower* and that of the $\boldsymbol{RC_{RD}}$ components is *higher*. These observations do indicate a correlation between location-dependent ST ductility and both microstructural features and microtextural characteristics in 12.7-cm-thick 2219-T87 plate.

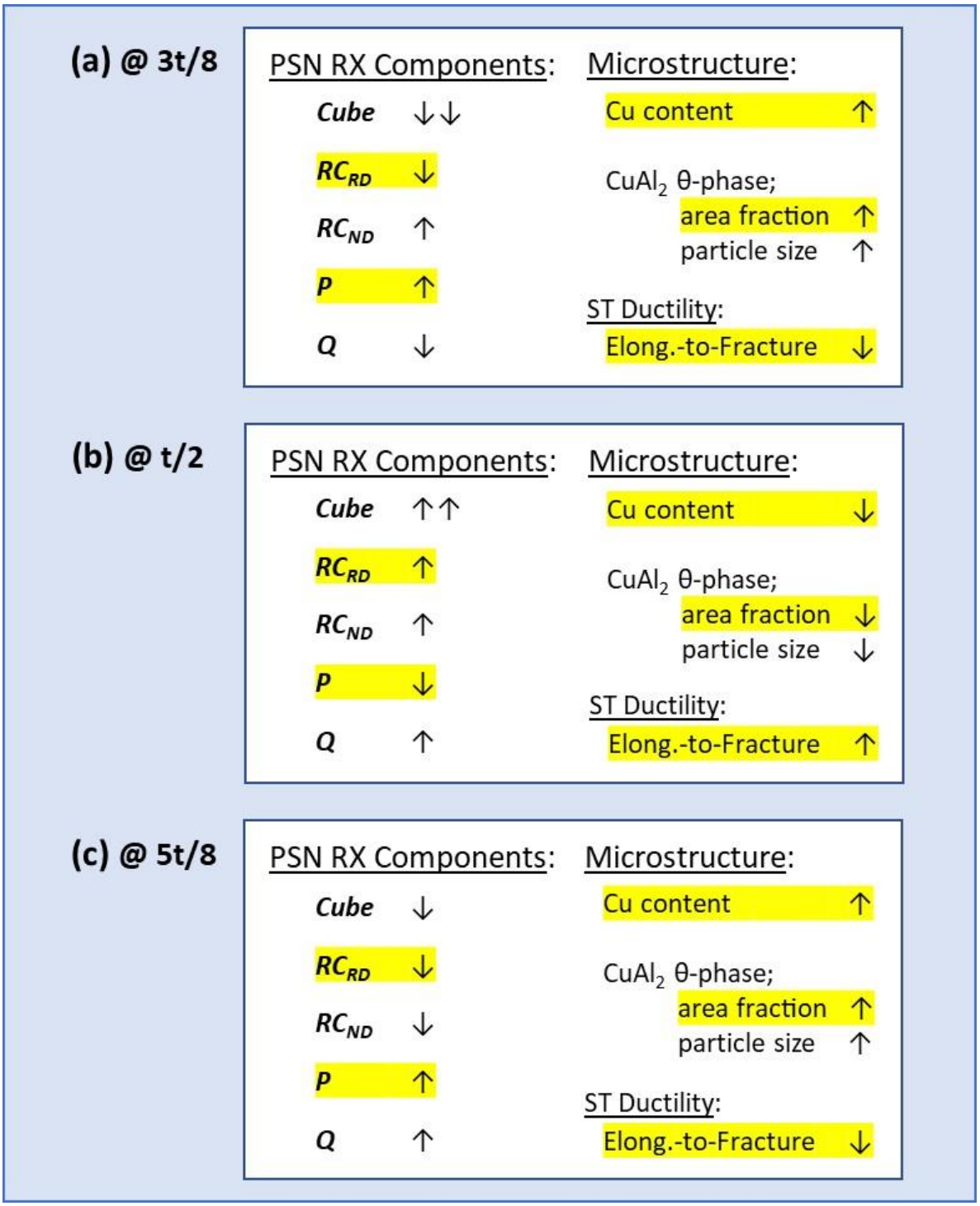

Figure 15. Illustration correlating through-thickness variations in PSN component intensities, microstructural characteristics and ST ductility in 12.7-cm-thick 2219-T87 plate: (a), 3t/8; (b), t/2; (c), 5t/8.

5.0 Conclusions

The outcome from this evaluation clearly indicates that the microtextural characteristics of the 12.7-cm-thick 2219-T87 plate studied (lot 930081-726) are asymmetrical through the cross section. Unfortunately, the 'top' and 'bottom' of the plate were not identified from the onset of this investigation. Although the through-thickness microtexture data is self-consistent, there is 180° ambiguity with respect to data from other sources. Consequently, any comparisons treat the data from the t/8 or 7t/8 locations, and the 3t/8 or 5t/8 locations, as interchangeable. This situation renders correlation of grain orientation and GB misorientation data with microstructural asymmetry, or fracture at and away from the mid-plane of the plate, less than definitive.

Despite this handicap, the EBSD analysis does reveal that the through-thickness variations in individual components follow complex profiles. In general, location-dependent decreases in DEF grain orientations tend to be countered by increases in REX grain orientations. The overall strength of the variable microtextural features is low, such that cross-sectional asymmetry may be classified as a second order effect on ST ductility or fracture behavior.

The detailed analyses of a single dataset demonstrate how preferred grain orientations, GB misorientations, and CSL boundaries might influence location-dependent fracture behavior. Even though the current results are considered exploratory, the novel analytical treatments employed may serve as a template for interpreting multiple datasets in future investigations. The current data highlight the consequences of microstructural asymmetry in Al alloy thick plate. Similar studies should prioritize compilation of microtextural data representative of the entire cross-section.

The microtexture data suggest that the most probable root cause of the cross-sectional variations is the Cu macro-segregation profile. The Cu content exceeds the maximum solid solubility limit of the alloy that causes the formation of equilibrium Al_2Cu θ-phase. The resulting distribution of coarse particles is inhomogeneous, which controls particle-stimulated nucleation during RX. The most significant outcome among the PSN-related texture category concerns the unique through-thickness variation of the ***P*** component (Miller indices; {011}<122>).

The area fraction of ***P*** oriented grains varies almost symmetrically about the mid-plane and the profile approximates the variation in Cu content through the plate. Although weak, this implies that the PSN mechanism of RX plays a role in the grain size/morphology, composition/spatial distribution of grain orientations, GB characteristics, and perhaps intergranular fracture susceptibility. Relevant to processing history, this suggests that casting practices exerted more influence than rolling procedures, particularly quenching and/or homogenization treatments.

6.0 References

1. J.J. Sidor, "Effect of hot band on texture evolution and plastic anisotropy in aluminium alloys," Metals (MDPI), vol. 11, no. 8, article ID 1310, 17 pp., 2021.
2. M.M.R. Jaradeh, ***The Effect of Processing Parameters and Alloy Composition on the Microstructure Formation and Quality of DC Cast Aluminium Alloys***, Ph.D. Dissertation, KTH, Stockholm, SWE, 46 pp., November 2006.
3. L. Swartzendruber et al., "Nondestructive evaluation of non-uniformities in 2219 aluminum alloy plate – relationship to processing," NBSIR Report 80-2069, U.S. Dept. of Commerce, 250 pp., December 1980 (NASA-CR-164596).

4. M. Tiryakioglu and R.T. Shuey, “Quench sensitivity of 2219-T87 aluminum alloy plate,” Mater. Sci. Eng., vol. A527, nos. 18-19, pp. 5033-5037, 2010.
5. D.G. Eskin, “Mechansisms and control of macrosegregation in DC casting,” ***Light Metals2014***, J. Grandfield (ed.), TMS, Warrendale, PA, pp. 855-860, February 1, 2014.
6. S.F. Harnish ….. and H. Weiland, “High-temperature mechanical behavior and hot rolling of AA705X,” Metall. & Mater. Trans., vol. 36A, no. 2, pp. 357-369, 2005.
7. H.J. Bunge, “Orientation of individual crystallites,” ***Texture Analysis in Materials Science – Mathematical Models***, Butterworths, London, 1st Edition, p. 23 & pp. 227-239, 1982.
8. S.J. Hales and R.A. Hafley, “Texture and anisotropy in Al-Li alloy 2195 plate and near-net-shape extrusions,” Mater. Sci. & Eng., Vol. A257, pp. 153-164, 1998.
9. O.V. Mishin, B. Bay, and D. Juul Jensen, “Though-thickness texture gradients in cold-rolled aluminum,” Metall. & Mater. Trans., vol. 31A, no. 6, pp. 1653-1662, 2000.
10. J. Sidor, A. Miroux, R. Petrov, and L. Kestens, “Microstructural and crystallographic aspects of conventional and asymmetric rolling processes,” Acta Mater., vol. 56, no. 11, pp. 2495–2507, 2008.
11. S. Wronski, B. Ghillianu, T. Chauveau, and B. Bacroix, “Analysis of textures heterogeneity in cold and warm asymmetrically rolled aluminium,” Mater. Charact., vol. 62, pp. 22-34, 2011.
12. O. Engler, M. -Y. Huh, and C.N Tomé, “A study of through-thickness texture gradients in rolled sheets,” Metall. & Mater. Trans., vol. 31A, no. 9, pp. 2299-2314, 2000.
13. E.M. Elgallad, Z. Zhang, and X.G. Chang, “Effect of quenching rate on precipitation kinetics in AA2219 DC cast alloy,” Physica B, vol. 514, no. 6, pp. 70-77, 2017.
14. O. Engler and V. Randle, ***Introduction to Texture Analysis – Macrotexture, Microtexture, and Orientation Mapping***, CRC Press, Boca Raton, FL, 2nd Edition, pp. 147-172, 2010.
15. J. Hirsch, "Annealing of aluminum and its alloys,” ***Heat Treating of Nonferrous Alloys***, ASM Handbook, G.E. Totten and D.S. MacKenzie (eds.), ASM International, Materials Park, OH, Vol. 4E, pp. 137-147, 2016.
16. F.J. Humphreys, “The nucleation of recrystallization at second phase particles in deformed aluminium,” Acta Metall., vol. 25, no. 11, pp. 1323-1344, 1977.
17. K. Lücke and O. Engler, "Effects of particles on development of microstructure and texture during rolling and recrystallization in f.c.c. alloys", J. Mater.Sci.& Tech., vol.6, no.11, pp. 1113-1130, 1990.
18. B.H. Frodal, S. Thomesen, T. Børvick, and O.S. Hopperstad, “On fracture anisotropy in textured aluminium alloys,” Int. J. Sol. & Struct., vol. 244-245, article ID 111563, 12 pp., 2022.
19. S.J. Hales and R.A. Hafley, “Texture/yield strength correlations in Al-Li near-net-shape extrusions,” Mater. Sci. Forum, vol. 331, pp. 1347-1352, 2000.
20. X. Yuan, K. Gao, G.S. Rohrer, and X. Fang, “Grain boundary plane distributions in a hot rolled 5A06 aluminum alloy,” Adv. Eng. Mater., vol. 6, no. 9, pp. 1105-1110, 2014.
21. J. Zhao and B.L. Adams, “Definition of an asymmetric domain for intercrystalline misorientation in cubic materials in the space of Euler angles,” Acta Cryst., vol. A44, no. 3, pp. 326-336, 1988.
22. A.D. Rollett, “Grain boundary engineering and concident site lattice theory,” Texture, Microstructure & Anisotropy lecture series, Mater. Sci. & Eng. Dept., Carnegie Mellon University, Pittsbugh, PA, 77 pp. 2016. http://pajarito.materials.cmu.edu/lectures/L14-CSL_Theory_GBE-17Mar16.pdf, accessed July 2022.

23. M.C. Messner, A.J. Beaudoin, and R.H. Dodds, Jr., “An interface compatibility/equilibrium mechanism for delamination fracture in aluminum–lithium alloys,” Eng. Fract. Mech., vol. 133, no. 1, pp. 70-84, 2015.
24. R. Dingreville, D. Aksoy, and D.E. Spearot, “A primer on selecting grain boundary sets for comparison of interfacial fracture properties in molecular dynamics simulations,” Scientific Reports (Nature), vol. 7, article ID 8332, 12 pp. 2017.
25. K.T. Aust, U. Erb, and G. Palumbo, “Interface control for resistance to intergranular cracking,” Mater. Sci. & Eng., vol. A176, nos. 1-2, pp. 329-334, 1994.
26. ***AZtecHKL*** software, Oxford Instruments, Concord, MA; https://nano.oxinst.com/products/aztec/aztechkl, accessed July 2022.
27. ***OIM*** software, EDAX LLC, Warrendale, PA; https://www.edax.com/products/ebsd/oim-analysis, accessed July 2022.
28. ASTM E2627-13, Standard Practice for Determining Average Grain Size Using Electron Backscatter Diffraction (EBSD) in Fully Recrystallized Polycrystalline Materials, November 1, 2019.
29. ISO 24173, Microbeam Analysis – Guidleines for Orientation Measurment Using Electron Backscatter Diffraction, September 1, 2009.
30. O. Engler, “An EBSD local texture study on the nucleation of recrystallization at shear bands in the alloy Al-3%Mg,” Scripta Mater., vol. 44, no.2, pp. 229-236, 2001.

Appendix A

The chart in Figure A1 depicts the texture asymmetry in the plate cross-section through a comparison of the microtextural composition and distribution at the t/8, $t/2_I$, and 7t/8 locations.

The chart Figure A2 depicts texture gradients related to common fracture locations through a comparison of the microtextural composition and distribution at the 3t/8, $t/2_{II}$, and 5t/8 locations.

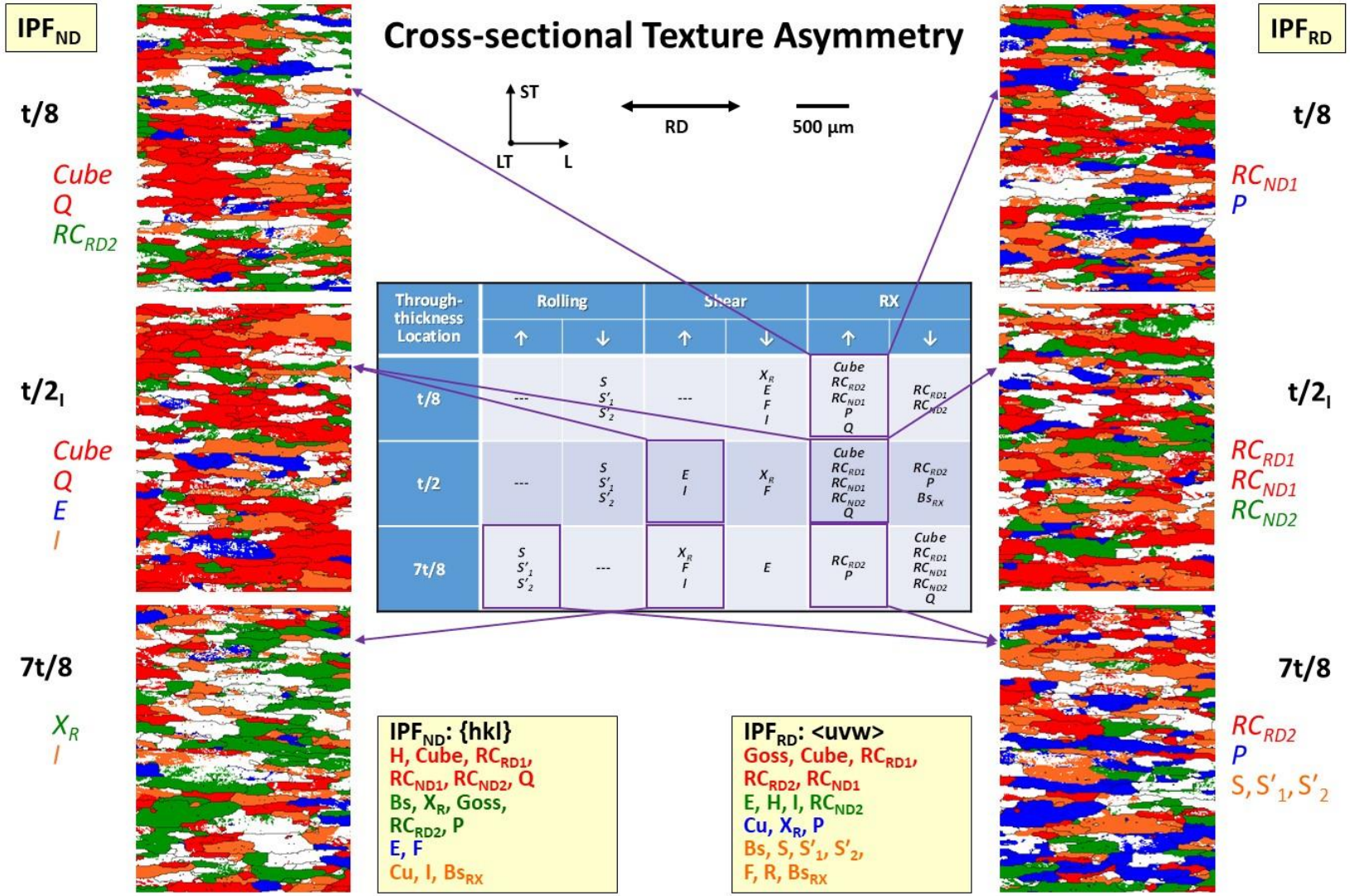

Figure A1. Variations in the textural composition and distribution of grain orientations at three through-thickness locations. Focusing on full-thickness microtexture asymmetry and disregarding other trends. Highlighting varying characteristics adjacent to the surfaces and comparing with the mid-plane.

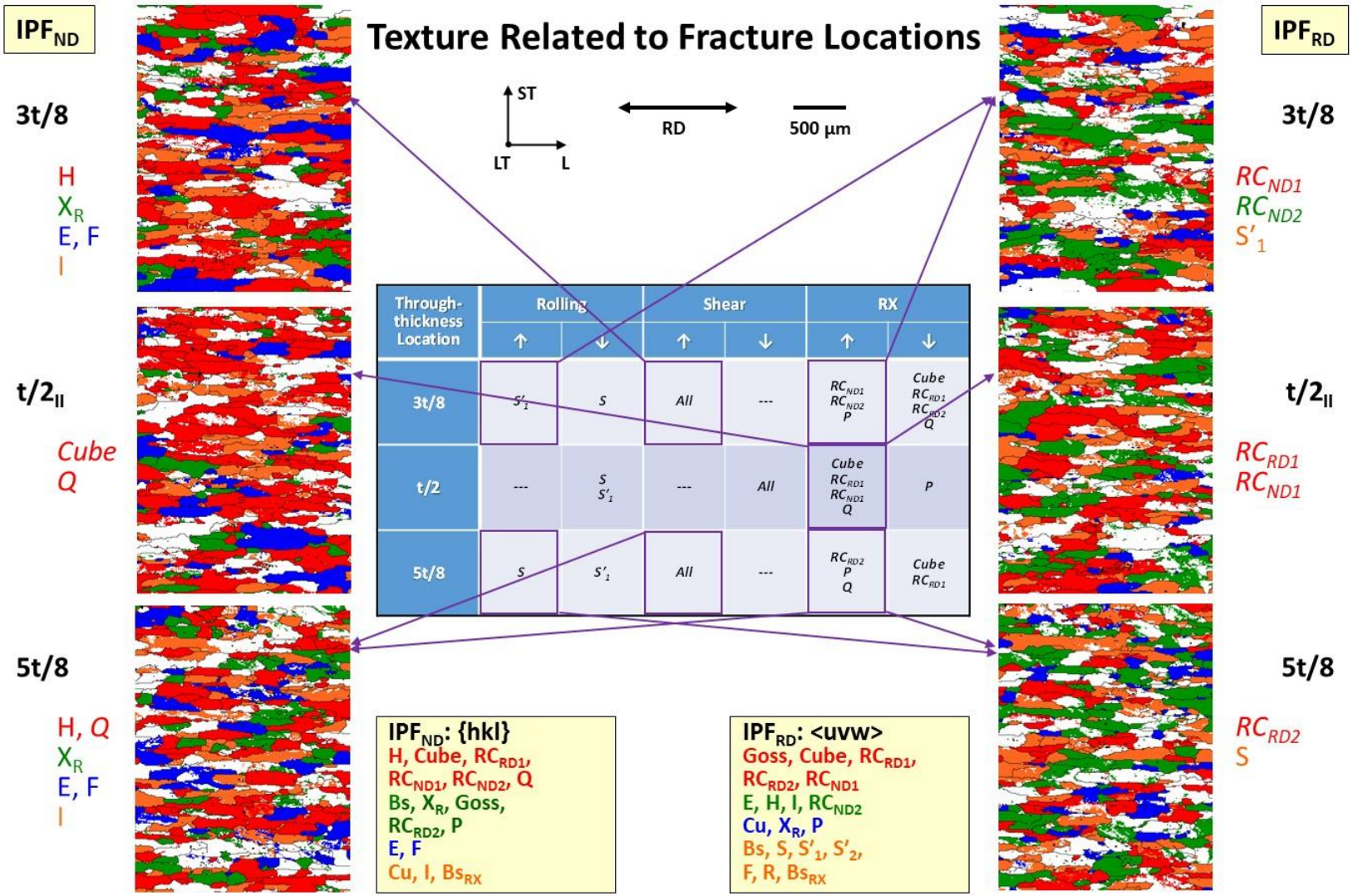

Figure A2. Variations in the textural composition and distribution of grain orientations at three through-thickness locations. Focusing on microtexture related to fracture locations and disregarding other trends. Highlighting varying characteristics away from the mid-plane and comparing with the mid-plane.

REPORT DOCUMENTATION PAGE

Form Approved
OMB No. 0704-0188

The public reporting burden for this collection of information is estimated to average 1 hour per response, including the time for reviewing instructions, searching existing data sources, gathering and maintaining the data needed, and completing and reviewing the collection of information. Send comments regarding this burden estimate or any other aspect of this collection of information, including suggestions for reducing the burden, to Department of Defense, Washington Headquarters Services, Directorate for Information Operations and Reports (0704-0188), 1215 Jefferson Davis Highway, Suite 1204, Arlington, VA 22202-4302. Respondents should be aware that notwithstanding any other provision of law, no person shall be subject to any penalty for failing to comply with a collection of information if it does not display a currently valid OMB control number.
PLEASE DO NOT RETURN YOUR FORM TO THE ABOVE ADDRESS.

1. REPORT DATE *(DD-MM-YYYY)*	2. REPORT TYPE	3. DATES COVERED *(From - To)*
04/21/2023	Technical Publication	

4. TITLE AND SUBTITLE
Evaluation of Through-thickness Microtextural Characteristics in 2219-T87 Thick Plate

5a. CONTRACT NUMBER

5b. GRANT NUMBER

5c. PROGRAM ELEMENT NUMBER

6. AUTHOR(S)
Hales, Stephen J.; Tayon, Wesley A.

5d. PROJECT NUMBER

5e. TASK NUMBER

5f. WORK UNIT NUMBER
869021.01.23.01.01

7. PERFORMING ORGANIZATION NAME(S) AND ADDRESS(ES)
NASA Langley Research Center
Hampton, VA 23681-2199

8. PERFORMING ORGANIZATION REPORT NUMBER
NESC-RP-21-01721

9. SPONSORING/MONITORING AGENCY NAME(S) AND ADDRESS(ES)
National Aeronautics and Space Administration
Washington, DC 20546-0001

10. SPONSOR/MONITOR'S ACRONYM(S)
NASA

11. SPONSOR/MONITOR'S REPORT NUMBER(S)
NASA/TP-20230006226

12. DISTRIBUTION/AVAILABILITY STATEMENT
Unclassified - Unlimited
Subject Category Metals and Metallic Materials
Availability: NASA STI Program (757) 864-9658

13. SUPPLEMENTARY NOTES

14. ABSTRACT
The objective of this investigation was to establish whether crystallographic texture played a role in variable ST ductility in 2219-T87 thick plate. The EBSD study involved data collection at NASA Glenn Research Center and ODF analysis of the imported data at NASA Langley Research Center. The most significant result was that through-thickness variations in microtextural characteristics were asymmetrical about the mid-plane of the plate. However, the overall texture intensity was low, such that cross-sectional variations were classified as a second order effect on ST ductility.

15. SUBJECT TERMS
Aluminum alloy; 2219-T87; Thick Plate; Segregation; Short-Transverse Properties; Microstructure; Texture

16. SECURITY CLASSIFICATION OF:			17. LIMITATION OF ABSTRACT	18. NUMBER OF PAGES	19a. NAME OF RESPONSIBLE PERSON
a. REPORT	b. ABSTRACT	c. THIS PAGE			STI Help Desk (email: help@sti.nasa.gov)
					19b. TELEPHONE NUMBER *(Include area code)*
U	U	U	UU	45	(443) 757-5802